JGR Solid Earth

RESEARCH ARTICLE
10.1029/2020JB019962

Key Points:

- We observe clear Ps and SP converted phases generated from the top and bottom of the oceanic crust of the subducted Gorda Plate
- Ps and SP converted phases are used to constrain the geometry of the interface of the subducted slab
- Amplitude of the converted phases indicates that the subduction plate interface is a low shear-wave velocity zone at seismogenic depth

Supporting Information:

- Supporting Information S1

Correspondence to:
Jianhua Gong,
jgong@whoi.edu

Citation:
Gong, J., & McGuire, J. J. (2021). Constraints on the geometry of the subducted Gorda plate from converted phases generated by local earthquakes. *Journal of Geophysical Research: Solid Earth*, *126*, e2020JB019962. https://doi.org/10.1029/2020JB019962

Received 17 APR 2020
Accepted 15 JAN 2021

Constraints on the Geometry of the Subducted Gorda Plate From Converted Phases Generated by Local Earthquakes

Jianhua Gong[1] **and Jeffrey J. McGuire**[2]

[1]MIT/WHOI Joint Program in Oceanography/Applied Ocean Science and Engineering, Woods Hole, MA, USA, [2]United States Geological Survey, Moffett Field, CA, USA

Abstract The largest slip in great megathrust earthquakes often occurs in the 10–30 km depth range, yet seismic imaging of the material properties in this region has proven difficult. We utilize a dense onshore-offshore passive seismic dataset from the southernmost Cascadia subduction zone where seismicity in the mantle of the subducted Gorda Plate produces *S*-to-*P* and *P*-to-*S* conversions generated within a few km of the plate interface. These conversions typically occur in the 10–20 km depth range at either the top or bottom of a ~5 km thick layer with a high Vp/Vs that we infer to be primarily the subducted crust. We use their arrival times and amplitudes to infer the location of the top and bottom of the subducted crust as well as the velocity contrasts across these discontinuities. Comparing with both the Slab1.0 and the updated Slab2 interface models, the Slab2 model is generally consistent with the converted phases, while the Slab1.0 model is 1–2 km deeper in the 2–20 km depth range and ~6–8 km too deep in the 10–20 km depth range between 40.25°N and 40.4°N. Comparing the amplitudes of the converted phases to synthetics for simplified velocity structures, the amplitude of the converted phases requires models containing a ~5 km thick zone with at least a ~10%–20% reduction in *S* wave velocity. Thus, the plate boundary is likely contained within or at the top of this low velocity zone, which potentially indicates a significant porosity and fluid content within the seismogenic zone.

1. Introduction

Paleoseismic studies of the Cascadia subduction zone demonstrate that it routinely generates M8–9 megathrust earthquakes (Atwater et al., 1995; Goldfinger et al., 2003) possibly with significant variability in their along-strike extents. However, due to the lack of instrumentally recorded large megathrust earthquakes, the extremely low rates of interplate seismicity, and the inadequate coverage of offshore geodetic observations, we lack a clear delineation of the likely rupture extent of future great earthquakes (Wang & Tréhu, 2016).

From geodetic observations, the Cascadia megathrust (subducted plate interface) is spatially segmented into an interseismically locked zone (Hyndman, 2013; Hyndman & Wang, 1995; McCaffrey et al., 2013; Pollitz & Evans, 2017; Schmalzle et al., 2014) that is likely confined to depths shallower than ~21 km (Bruhat & Segall, 2016), a region of episodic tremor and slow slip (ETS) at depths between ~30 and 50 km (Rogers & Dragert, 2003; Wang & Tréhu, 2016; Wech & Creager, 2011), and an intervening transition zone with uncertain rupture potential (Liu, 2013; Ramos & Huang, 2019). Current hazard models implement three possible scenarios where earthquakes are either contained largely offshore, propagate far onshore to reach the ETS zone, or terminate within the transition zone (Petersen et al., 2014; Wirth et al., 2018). These scenarios predict significantly different impacts on the overlying regions. Thus, whether future great earthquakes that initiate within the locked zone can rupture through the transition zone has considerable consequences for earthquake risk in large cities such as Seattle, Tacoma, Portland, and Vancouver. A better understanding of the likely downdip extent of future ruptures requires detailed information on the material properties and physical conditions of the plate boundary zone at depths of 10–30 km.

It is well established that both the shallow and deep parts of subduction megathrusts are weak faults. Direct observations of high pore fluid pressures (Saffer & Tobin, 2011) and low friction coefficients of recovered core samples (Fulton et al., 2013) indicate the shallow megathrust often has an effective friction coefficient less than 0.1. Similarly, both receiver function imaging studies and dynamic triggering of tremor suggest that the ETS zone is characterized by near lithostatic pore fluid pressures (Audet et al., 2009; Liu & Rice, 2005;

Rubinstein et al., 2007). Moreover, modeling studies of ETS behavior in Cascadia require a contrast of a factor of ∼50 in effective normal stress between the downdip ETS zone and the seismogenic zone (Liu & Rice, 2007; Segall & Bradley, 2012) suggesting that the zone of high fluid pressure does not extend into the locked zone. Moreover, increases in earthquake stress drop from ∼5–30 km depth (Bilek & Lay, 1999) and the strong high-frequency radiation from the deeper parts of large ruptures (Lay et al., 2012) indicate that shear stress on the megathrust is highest at the downdip end of the seismogenic zone. Understanding these along dip variations in physical conditions, particularly in the depth range where coseismic slip is expected to be greatest (10–30 km), may help us understand the level of shaking to expect in future great earthquakes.

The geometry and physical properties of the Cascadia megathrust are well imaged at shallow depths by offshore active-source seismic experiments and also at depths of ∼30–50 km, albeit with lower resolution, using onshore teleseismic methods. Han et al. (2017) demonstrated differences in the consolidation state of the sediments in the accretionary wedge are correlated with variations in coupling between the portions of the plate boundary offshore of Oregon and Washington. Their images extended to about 6 km below the seafloor. Similarly, Peterson and Keranen (2019) imaged porosity variations in the fault-zone down to about 3 km depth below the seafloor. A few active source reflection studies have been able to characterize the plate boundary zone to great depths. Nedimović et al. (2003) showed that within the seismogenic depth range (∼10–20 km) the plate boundary zone is characterized by a 2 km wide (or less) zone of sediments while at the depths of ETS events the plate boundary zone expands to a width of over 4 km. Onshore seismic experiments that utilized teleseismic data imaged the ETS zone as a ∼5–10 km thick region of low shear-wave velocities (vs.) and a high ratio of compressional to shear-wave seismic velocities (Vp/Vs) that indicates extremely high fluid content and inferred fluid pressure (Abers et al., 2009; Audet et al., 2009; Peacock et al., 2011; Tauzin et al., 2017). The high fluid content of the ETS zone is corroborated by magnetotelluric inversions that show strongly conductive regions immediately above the slab in the 30–40 km depth range (Evans et al., 2014; McGary et al., 2014; Wannamaker et al., 2014).

The intervening depth range from 5 to 30 km depth has been less well imaged owing to its combination of being located primarily offshore and at significant depth. Beaudoin et al. (1994) imaged the subducted Gorda crust with an onshore refraction line in our study area and concluded the top of the subducted plate is at approximately 14 km depth in their along-strike line located near the coast. They found that the subducted crust was characterized by *P* wave velocities from 6.2 to 6.7 km/s and is 7–10 km thick. They found some possible evidence for subducted sediments near the top of the crust but concluded that no low velocity zone was required to fit their data. Their preferred model generated reflections from a 6.0–6.7 km/s discontinuity in Vp at the top of the crust as well as from a 6.7–7.7 km/s discontinuity in Vp at the base of the subducted crust corresponding to ∼10%–15% velocity increases. Beaudoin et al. (1998) imaged the subducted Gorda crust between 20 and 30 km depth with a northwest-southeast oriented wide-angle reflection profile. The top of the subducted Gorda crust is characterized as intermittent sharp reflection interfaces with segmented thin high-reflectivity regions on top of the crust. The oceanic Moho of the subducted plate has the brightest reflection.

Recently, several local earthquake tomography studies and large-scale community velocity models provided more detailed information on the structure of the Cascadia subduction zone at depths of 10–30 km. Using published geophysical data in addition to borehole and other geological constraints, Stephenson et al. (2017) constructed 3D *P* and *S* wave velocity models for large-scale ground motion simulations in Cascadia. Guo et al. (2018) imaged the subduction zone structure near the Mendocino triple junction (MTJ) area where the subducting Gorda plate crust is characterized as a high Vp/Vs (∼1.85) layer about 6 km thick. They interpreted this layer as the subducted oceanic crust. The high Vp/Vs ratio indicated a significant porosity (few percent) within the depth range of interseismic locking. They estimated the depth of the crust to be slightly (1–2 km) deeper than in the model of Beaudoin et al. (1994). They also found a reduction in Vp/Vs and hence decrease in porosity in the geodetic transition zone. They interpreted the spatial variations in Vp/Vs ratio as indicating that the transition zone is governed by a ductile rheology that would inhibit significant onshore propagation of large ruptures. Similarly, Savard et al. (2018) imaged the forearc area beneath northern Cascadia in the 20–40 km depth range which revealed a high Poisson's ratio suducted upper oceanic crust and a low Poisson's ratio forearc continental crust above the mantle wedge, suggesting an association between composition, fluids, and seismogenesis. Both tomographic studies covered regions of

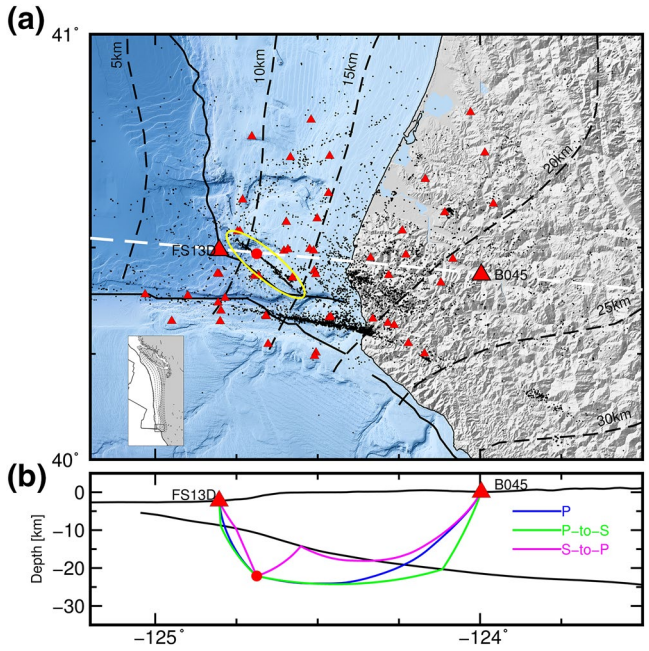

Figure 1. Map of the study area and a cross section showing the raypaths of converted phases. (a) Red triangles denote seismic stations. Black dots denote earthquake locations from Guo et al. (2018). Bold black lines denote plate boundaries from the USGS Quaternary Fault and Fold Database. Black dash lines denote the Gorda slab depth contours from the Slab1.0 model. The white dash line denotes the cross section shown in (b). Topography and bathymetry data are from the NOAA Coastal Relief Model and ETOPO1 Global Relief Model. The earthquakes inside the yellow ellipse occur primarily on a fault in the mantle of the downgoing plate (termed the M-Fault) which was analyzed in Chen and McGuire (2016). The inset map shows the Cascadia subduction zone. Our study area is shown as the black rectangle at the southern end of Cascadia. (b) Blue, green, and magenta lines are raypaths of the P, Ps, and Sp phases from one M-fault earthquake to one onshore (B045) and one offshore (FS13D) station. The thin black line denotes topography along the cross section and the bold black line denotes the plate boundary geometry from the Slab1.0 model (McCrory et al., 2012).

Cascadia with sufficient local earthquake data to improve the constraints on structure near the downdip edge of interseismic locking.

Most traditional passive source seismic imaging methods, such as receiver functions and first-arrival tomography, produce images with inherently low resolution and have difficulty with seafloor seismic data. Teleseismic receiver functions are typically calculated using 0.1–1 Hz waves, which sets a coarse spatial resolution (∼5–10 km) relative to the geologic structures associated with a plate boundary fault. Analyzing the seafloor seismic data collected above the locked zone from the Cascadia Initiative dataset (Toomey et al., 2014) with the receiver function method, Janiszewski and Abers (2015) found evidence for a strong low velocity zone at plate boundary depths from primarily one high quality station, while a stacked image of the whole dataset from Audet and Schaeffer (2018) found that the low velocity zone seen at ETS depths was absent in the seismogenic depth range. Similarly, tomographic velocity models are inherently smooth and often do not resolve a low velocity zone in the vicinity of the plate boundary owing to its short spatial scale despite the high probability that such a zone exists due to the subducted melange layer. A key question for understanding the physical properties and the intensity of shaking that should be expected in Cascadia is whether the deepest part of the locked zone (∼10–20 km) is characterized by high fluid pressure and hence a significant low velocity zone (LVZ). These conditions would imply lower values of the effective stress levels on the plate interface and perhaps weaker seismic radiation than models without a LVZ. Resolving these questions requires imaging methods with high resolution both in depth and laterally that can detect the physical properties of the plate boundary zone at depths of ∼20 km.

In this paper, we use *S*-to-*P* and *P*-to-*S* phases generated by local earthquakes in the mantle of the downgoing plate and converted in the vicinity of the slab interface to constrain the depth and material properties of the plate boundary zone. These type of phases have been used for imaging the structure of subducted slabs in a number of regions including: Japan (, 1990; Horleston & Helffrich, 2012; Matsuzawa et al., 1986; Nakamura et al., 1998; Obara & Sato, 1988; Ohmi & Hori, 2000), New Zealand (Eberhart-Phillips & Reyners, 1999; Reading et al., 2001), Mexico (Lomnitz, 1982; Song et al., 2009; Song & Kim, 2011), Alaska (Stephens et al., 1990), and Cascadia (Merrill & Bostock, 2019; Nowack & Bostock, 2013). These types of converted phases typically have high-frequency content (1–15 Hz) and are able to create sharper images of the interface. Most of the above studies focus on the slab structure below 30 km depth. We take advantage of the high seismicity rate near the Mendocino triple junction and a dense onshore-offshore seismic array to study the slab interface structure from 10 to 20 km depth in the anticipated seismogenic zone. The combination of the high-frequency nature of the local earthquake generated converted phases and the dense seismic array allows the potential to study rapid variations in the material properties both in depth and laterally on a scale that matches the variations in geodetic observations of interseismic coupling.

2. Data

We utilize seismic data from an onshore-offshore network near the MTJ which includes 39 temporary OBS stations, 10 temporary onshore stations, and 7 permanent onshore stations (Figure 1). The OBS stations were deployed during the Cascadia Initiative (CI) experiment (Toomey et al., 2014) and included instruments from the Lamont-Doherty Earth Observatory (LDEO), the Scripps Institution of Oceanography

(SIO), and the Woods Hole Oceanographic Institution (WHOI). They were deployed during two time periods: 2012–2013 and 2014–2015 (Year 2 and Year 4 in the CI experiment) with slightly different station configurations. All of the OBS stations included three component broadband seismometers and most were equipped with either an absolute or differential pressure gauge. Instrument types and their sampling rates are different between the three institutions. The data duration and quality is better in Year four than Year two due to a number of factors. The pressure sensors at deep water stations were used in our analysis but the oceanographic noise levels at shallow water stations (<500 m depth) prevented us from using those records. The 10 temporary onshore stations were short-period sensors from the IRIS-Portable Array Seismic Studies of the Continental Lithosphere (PASSCAL, 2014–2015). The seven permanent stations were from broadband stations of the Northern California Seismic Network and the Berkeley Digital Seismic Network, and the short-period borehole stations of the UNAVCO Plate Boundary Observatory.

Waveforms for each earthquake are windowed between 1 min before and 2 min after the origin time. The waveforms are filtered between 1 and 5 Hz, 2 and 7 Hz, or 4 and 12 Hz to identify which frequency band yields the most easily visible converted phases on a particular component. Noisy data for particular earthquakes are then removed from the dataset based on their signal-to-noise ratio for the direct waves. *P* and *S* wave arrivals are repicked by cross correlation and then manually shifted if cross correlation does not yield satisfactory alignment results within a record section.

We utilize earthquake location results and tomography models from Guo et al. (2018) which were determined with the same seismic array. In this study, we focus on events in the yellow ellipse in Figure 1 because those events naturally form a source array with similar waveforms. The earthquakes occurred at about 25 km depth on a strike-slip fault in the subducted oceanic mantle (hereinafter referred as the M-fault). They are shallower to the west and deeper to the east, and the relocated dataset contains about 450 events which are recorded to various degrees by the different stations depending on their duration of recording. We use the Slab1.0 model from McCrory et al. (2012) as a reference slab geometry model as well as for calculating raypaths and arrival times of the different converted phases.

3. Methods

In this section, we demonstrate how to identify *S*-to-*P* and *P*-to-*S* converted phases generated near the plate boundary interface on seismic record sections. The *S*-to-*P* and *P*-to-*S* converted phases arrive in between the direct *P* and *S* waves. We use raytracing and the source side beamforming method to identify and classify these converted phases. We also apply the wavefield decomposition method to remove water reflection phases on OBS records. Examples of *P*, *S*-to-*P* and *P*-to-*S* raypaths from an M-fault earthquake to both onshore and offshore stations are shown in Figure 1b).

3.1. Raytracing

To calculate *S*-to-*P* and *P*-to-*S* traveltimes and the locations of the conversion points on the slab interface, we apply a 3D raytracing method to each event-station pair using the *P* and *S* wave velocity models from Guo et al. (2018). The raytracing code is extracted from the TomoDD software (Zhang & Thurber, 2003), which is based on the pseudoray bending method described in Um and Thurber (1987). Since the smooth tomographic velocity models do not contain discontinuities to generate converted phases, we trace rays that travel as a *P* (or *S*) wave from the event to Slab1.0 model interface and travel as *S* (or *P*) wave from slab interface to station. We mesh the slab interface into a 1×1 km grid and then calculate raypaths and traveltimes from the event to the slab surface grid points and from the grid points to the station. We then identify the grid point that yields the minimum total traveltime as the conversion point. For *S*-to-*P* converted phases, two types of raypaths exist: transmission (e.g., FS13D in Figure 1b) and reflection refraction (e.g., B045 in Figure 1b). The latter occurs when the station is far away enough that the *S*-to-*P* conversion phase reaches the total reflection condition (see supplementary information). This is not the case for *P*-to-*S* converted phases as the *S* wave velocity is always smaller than *P* wave at the conversion point and the *S* wave part of the ray will always go upward. By traditional naming convention in seismology, we will use Ps to represent *P*-to-*S* converted phase from now on for simplicity. And we will use SP to represent *S*-to-*P* converted phases

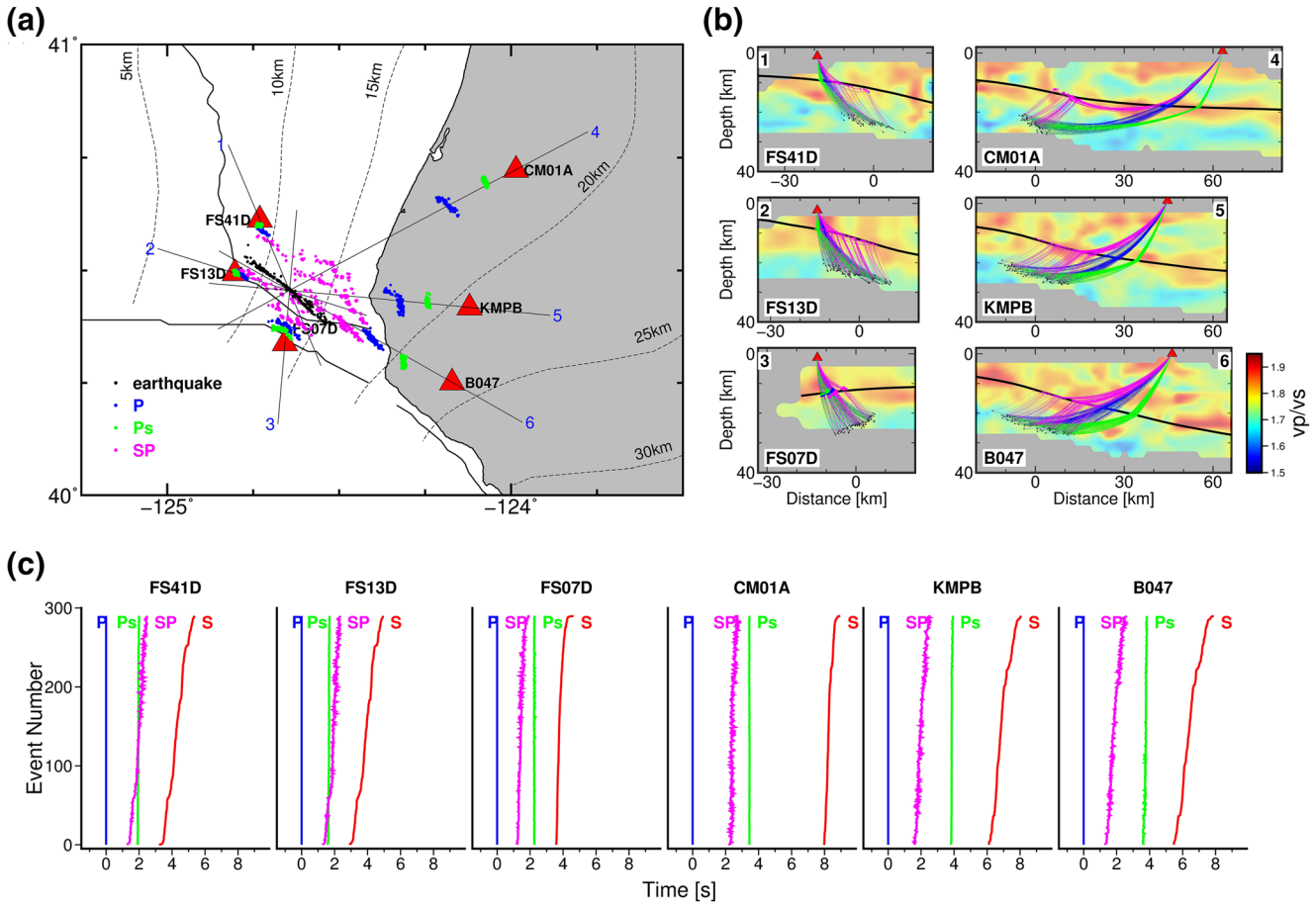

Figure 2. Raytracing results. (a) Location of Ps (green) and Sp (magenta) conversion points and direct *P* (blue) wave piercing points on the slab interface from M-Fault events to stations FS41D, FS13D, FS07D, CM01 A, KMPB, and B047. Lines 1–6 are locations of the cross sections shown in (b). The six cross sections connect the center of the M-Fault events with each station. (b) Cross sections going through the center of the M-Fault events to each station. The background color denotes the Vp/Vs ratio model from Guo et al. (2018). Black dots denote the locations of the M-Fault earthquakes. Blue, green and magenta lines denote P, Ps, and Sp phase raypaths. Blue, green, and magenta dots denote P, Ps, and Sp phase piercing/conversion points on the slab interface. Black lines and red triangles denote the subduction interface geometry and seismic stations. Earthquake locations, piercing/conversion points, and raypath are projected onto each cross section. (c) Predicted P (blue), Ps (green), Sp (magenta), and S (red) phases traveltime curves for each station from the M-Fault events. Traveltime curves are aligned on the direct P arrival. The vertical axis is event order sorted by the *S-P* traveltime difference.

of both the transmission type and the reflection refraction type. We use the Slab1.0 model instead of the Slab2 model (Hayes et al., 2018) because Slab2 does not cover a large enough area offshore to calculate piercing/conversion points of the P, S, Ps, and SP phases for some OBS stations. However, we compare our converted phases results with both the Slab1.0 and Slab2 models in the Discussion section. We validated the minimum traveltime path ray tracing approach for the Ps and SP phases using 2D waveform simulations (Tromp et al., 2008) for our velocity model (see supplementary information).

Several raytracing results are shown in Figure 2 that demonstrate the general features of our dataset. Compared to *P* wave piercing points, Ps conversion points are closer to the station and are more concentrated, while SP conversion points are farther away from the station and are spread out over a much larger area for a given set of earthquakes. On the traveltime plots (Figure 2c), Ps phases have a similar moveout to the direct *P* wave while SP phases show a moveout that is intermediate between the *P* and *S* wave moveouts but with more scatter. Figure 3a compares the predicted SP arrival times to a vertical component record section at station CM01 A. The seismograms are aligned on the *P* wave and ordered by their *S-P* traveltime difference. The blue line is the predicted traveltime of the SP converted phases. Large amplitude arrivals can be seen close to the predicted arrival time for many earthquakes and the conversion points of the SP phases

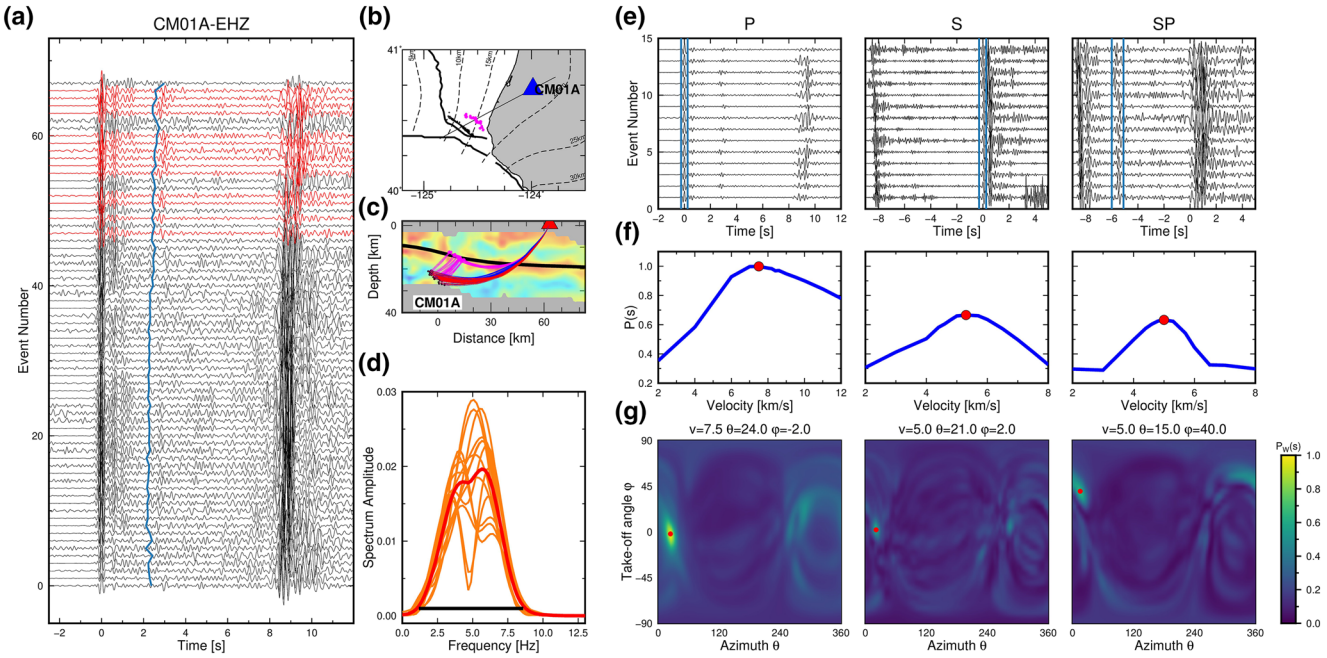

Figure 3. Waveform section and source side 3D beamforming results for station CM01 A. (a) Z component seismograms from M-Fault events. The seismograms are aligned by the *P* wave and sorted by the *S-P* traveltime difference. Red traces are the ones used for beamforming analysis. The blue line denotes the predicted arrival time of SP phase converted at the Slab1.0 model. (b) Map view of the location of the M-Fault events and station CM01 A. (c) Raypaths of P, S, and SP (reflection refraction type) phases from the M-fault events to station CM01 A. The background colors denote the Vp/Vs model as in Figure 2. (d) Orange lines show the power spectrum of each SP converted phase from the red traces in (a) and the red line is the averaged power spectrum. The horizontal black line represents the selected frequency range for the beamforming analysis. (e) Waveform section of the selected traces in (a) with the blue lines denoting the selected windows for P, S, and SP phase for beamforming analysis. In the first panel, the seismograms are aligned by the *P* wave. In the second and third panels, the seismograms are aligned by the *S* wave. All the seismograms are sorted by *S-P* traveltime difference. (f) Maximum slowness power spectrum as a function of velocity. The maximum value is marked by the red dot. (g) Slowness power spectrum as a function of azimuth and takeoff angle for the best velocity estimate in (f). The location of the maximum of the slowness power spectrum is marked by the red dots and the best velocity, azimuth (θ) and takeoff angle (ϕ) are shown in the title of each panel.

and the raypaths are shown in Figures 3b and 3c. To further establish that these large amplitude signals are SP converted phases, we apply the source side beamforming method described below.

3.2. Source Side beamforming

The clear arrivals between the direct P and S phases are suggestive of converted phases and we confirm the sense of the conversion (Ps or SP) using a source side 3D beamforming method (Nakata & Shelly, 2018; Spudich & Bostwick, 1987) and estimate the propagation directions and velocities of theses phases as they leave the earthquake source region. This method uses the reciprocity theory of wave propagation by viewing the seismograms recorded at a single station from a cluster of nearby earthquakes with similar waveforms as being identical to waveforms that would be generated by an earthquake that occurred at the location of the station and was recorded by an array of receivers at the position of the earthquakes. The beamforming method results in estimates of the near source velocities as well as the azimuth and the takeoff angles of the raypaths of the waves as they leave the earthquake source region.

The beamforming method may be described mathematically, as noted in Spudich and Bostwick (1987), let $\mathbf{r}_j$ be the relative location of event j from a reference location and $u(\mathbf{r}_j, t)$ be the wavelet of a certain phase from event j with zero time corresponding to the origin time of each earthquake. Applying a plane-wave decomposition, the complex amplitude in the slowness and frequency domain for N clustered earthquakes is:

$$\tilde{u}(\mathbf{s},\omega) = \frac{1}{N}\int_{-\infty}^{\infty} \sum_{j=1}^{N} u(\mathbf{r}_j,t) e^{i(\omega \mathbf{s}\cdot\mathbf{r}_j - \omega t)} dt \quad (1)$$

where **s** is the slowness vector of the outgoing rays and ω is angular frequency. The corresponding power spectrum is:

$$P(\mathbf{s},\omega) = \tilde{u}(\mathbf{s},\omega)u^{*}(\mathbf{s},\omega) \tag{2}$$

where $u^{*}(\mathbf{s}, \omega)$ is the complex conjugate of $\tilde{u}(\mathbf{s},\omega)$. Following Equation 1, we have

$$\begin{aligned}\tilde{u}(\mathbf{s},\omega) &= \frac{1}{N}\sum_{j=1}^{N} e^{i\omega\mathbf{s}\cdot\mathbf{r}_j}\int_{-\infty}^{\infty} u(\mathbf{r}_j,t)e^{-i\omega t}dt \\ &= \frac{1}{N}\sum_{j=1}^{N} e^{i\omega\mathbf{s}\cdot\mathbf{r}_j}\mathcal{F}_j(\omega)\end{aligned} \tag{3}$$

where $\mathcal{F}_j(\omega)$ is the Fourier transform of event j. Ideally if we assume that the shape of the wavelets of different events are identical and the phase velocity near the source is nondispersive, the difference between the various $\mathcal{F}_j(\omega)$ is just a phase shift $e^{-i\omega\mathbf{s}_{real}\cdot\mathbf{r}_j}$ caused by the traveltime delay of each event from the reference point, and this phase shift will be compensated by the term $e^{i\omega\mathbf{s}\cdot\mathbf{r}_j}$ in Equation 3 when the true slowness is used. Hence, the true slowness is identified by finding the slowness that maximizes $\tilde{u}(\mathbf{s},\omega)$ for the summation over N events in Equation 3.

For nondispersive waves, the peaks of $P(\mathbf{s}, \omega)$ are independent of frequency, which suggests that stacking the power spectrum in Equation 2 over many frequencies along lines of constant slowness will enhance the resolution of the true slowness. Thus, the slowness power spectrum is defined as:

$$P(\mathbf{s}) = \frac{1}{M}\sum_{j=1}^{M} P(\mathbf{s},\omega_j) \tag{4}$$

where ω_j is the set of frequencies at which the power spectrum has been calculated. The slowness resolution can be further enhanced by whitening the spectrum in a frequency band where signal-to-noise ratio is favorable so that power in weak frequencies is equal to the power in the strong frequencies. The whitening factor w_j for frequency ω_j is given by:

$$w_j = \max_{\mathbf{s}}\{P(\mathbf{s},\omega_j)\} \tag{5}$$

and the whitened slowness power spectrum is

$$P_W(\mathbf{s}) = \frac{1}{M}\sum_{j=1}^{M}\frac{1}{w_j}P(\mathbf{s},\omega_j) \tag{6}$$

To apply this method with real data, we first align the waveform section by the direct P wave for potential Ps converted phase and by direct S wave for potential SP converted phase. Then a narrow window is cut around the wavelet of the converted phase. Each wavelet is normalized by its maximum amplitude and a Hann window is used to taper the wavelet. The wavelets are then shifted back to their arrival time. To choose a favorable frequency band, we first calculate the power spectrum of each wavelet and average them. The frequency band is chosen between the start and end frequencies where the average power spectrum stays above 5% of its maximum value (Figure 3). The slowness vector is represented in spherical coordinates as $\mathbf{s} = \left[\cos\phi\cos\theta / v, \cos\phi\sin\theta / v, \sin\phi\sin\theta / v\right]^{T}$, where ϕ is the takeoff angle ranging −90° to 90° from downward to upward, θ is azimuth angle ranging from 0° to 360° from eastward counterclockwise and v is the near source velocity. The slowness vector that yields the maximum whitened slowness power spectrum is used to estimate the wave propagation direction and velocity within the earthquake focal region. If the wavelets selected are indeed a Ps or SP converted phases, the estimated velocity, azimuth and takeoff angle should be consistent with the tomographic results for P or S wave velocity at the earthquake source location, the relative locations between the earthquakes and the station, and the raytracing results, respectively.

Figure 3 shows the beamforming results for the P, S, and the potential SP phases generated by a cluster of events near the western end of the M-Fault and recorded by station CM01 A. Figure 3e shows the selected wavelet for P, S, and SP phases. Figure 3f shows the maximum whitened slowness power spectrum as a function of velocity with the best estimate marked by the red dot. Figure 3g shows the beamforming results at the full range of takeoff angles and azimuths associated with the peak velocity estimation in Figure 3f. For P, S, and the potential SP converted phases, the best velocity estimates are 7.5 km/s, 5.0 km/s, and 5.0 km/s, respectively. Comparing to the tomographic results, where the *P* wave velocity is 8.2 km/s and the *S* wave velocity is 4.8 km/s at the source location, the beamforming yields a reasonable estimate. The azimuth estimations, which are 24° for P, 21° for S, and 15° for SP, are within 6° of the 21° azimuth calculated from the earthquake and station locations. The takeoff angle is near zero for P and S phases, but is 40° for SP phase, which is consistent with the raytracing results shown in Figure 3c. The comparison between the beamforming estimates and the more direct measurements are listed in Table S1. Thus, the beamforming confirms that the potential SP phases leave the earthquake source region with the *S* wave velocity and propagate upward (unlike the direct *S* wave which leaves nearly horizontally). Given that the traveltime of this phase is also close to the predicted arrival time, we identify it as a SP phase converted in the vicinity of the subduction interface.

3.3. Wavefield Decomposition

Seismograms from OBS stations usually contain high-amplitude phases resulting from reflections at the sea surface and in our dataset the SP phases at deep water (1,000–2,500 m) stations have similar arrival times to the water surface reflected phase. The amplitude of the water phase is usually larger than that of the SP phases making it difficult to analyze the converted phases on raw OBS seismograms. Here we use the dual sensors wavefield decomposition method (Amundsen & Reitan, 1995) to remove the water reverberation phase and improve the visibility of the SP phases.

For wave propagation in an isotropic, plane-layered medium resulting from a point source, within each layer the wavefield (pressure, stress, displacement or velocity) can be decomposed into upgoing and downgoing cylindrical waves propagating with *P* or *S* wave velocities (Aki & Richards, 2002). A schematic decomposition of the wavefield is shown in Figure 4. Here we consider the water layer above the seismometer as layer one and the sediment layer below the seismometer as layer 2. Amundsen and Reitan (1995) showed that the pressure field P in the water layer and the stress tensor component σ_{zz} in the sediment layer can be decomposed into upgoing and downgoing components, U_1^P, D_1^P, $U_2^{\sigma_{zz}}$, and $D_2^{\sigma_{zz}}$ using pressure and velocity records from a pressure gauge and seismometer installed at the same ocean bottom station. Since the water reverberation phases reach the seafloor from above, they are not present on the $U_2^{\sigma_{zz}}$ component. A full expression of the decomposition can be found in Amundsen and Reitan (1995), while the expression can be greatly simplified if the wave is propagating vertically as:

$$D_1^P = \frac{1}{2}P - \frac{\rho_1 \alpha_1}{2} v_z \tag{7}$$

$$U_2^{\sigma_{zz}} = -\frac{1}{2}P - \frac{\rho_2 \alpha_2}{2} v_z \tag{8}$$

where ρ_1, α_1, ρ_2, and α_2 are density and *P* wave speed in the water and sediment layer and v_z is the vertical velocity. Here we use $\rho_1 = 1.0 \times 10^3$ km/m^3, $\alpha_1 = 1.5$ km/s. In practice, the pressure sensor is usually biased by a constant calibration factor. Equation 7 is used to estimate the calibration factor by minimizing the energy on the D_1^P component before the water reverberation phase (Figure 4c, bottom left). Then Equation 8 is used to remove the water reverberations by grid searching for the (best) value for $\rho_2\alpha_2$ that minimizes the energy of the water reverberation phase on the $U_2^{\sigma_{zz}}$ component (Figure 4c, bottom right). When processing the real data, we first remove the instrument response to transform the waveforms into data with physical units (velocity: m/s; pressure: Pa). Both the velocity and pressure records are upsampled to 200 Hz if the sampling rates are different on the two instruments at a particular station.

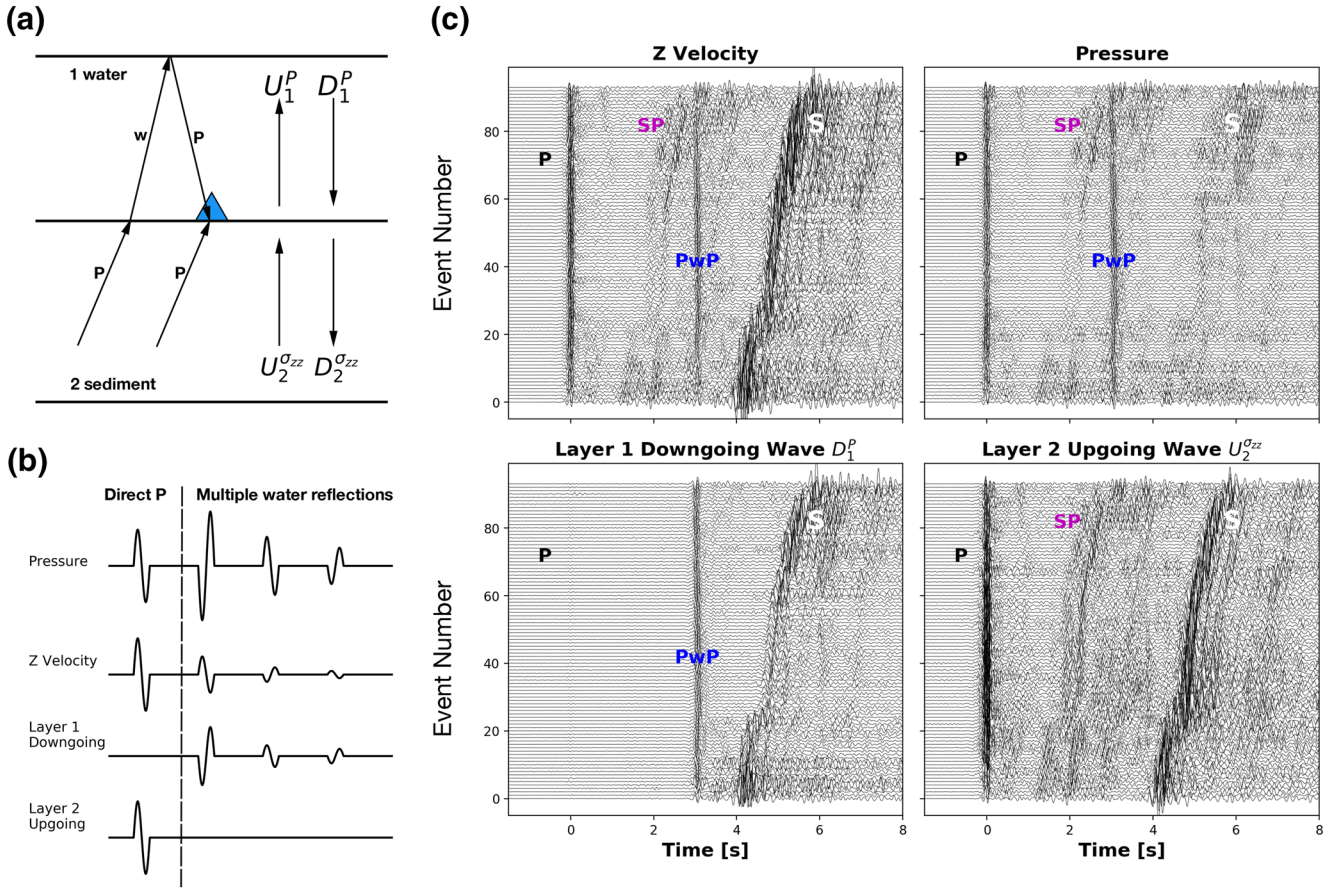

Figure 4. Wavefield decomposition results. (a) Schematic raypaths of the direct *P* wave and water reflection phase (PwP) recorded by an OBS (blue triangle) at the boundary between the upper water layer and the lower sediment layer. The pressure in the water layer and the stress component σ_{zz} in the sediment layer can be decomposed into upgoing (U_1^P, $U_2^{\sigma_{zz}}$) and downgoing (D_1^P, $D_2^{\sigma_{zz}}$) wavefields. (b) A conceptual plot showing the pressure and vertical velocity records of the direct P and multiple water reflection phases on an OBS station and the decomposed downgoing pressure field in the water layer and the upgoing stress (σ_{zz}) field in the sediment layer. This plot is modified from Thorwart (2006). (c) Wavefield decomposition results for station FS13D from the M-Fault events. P, S, SP (mixed transmission and reflection refraction types), and PwP phases are labeled on the record sections. The top two panels are vertical velocity and pressure records. The bottom two panels show the results for the decomposition into the downgoing pressure wavefield in the water layer (left) and upgoing stress (σ_{zz}) wavefield in the sediment layer (right). The seismograms are aligned by *P* wave and are sorted by *S-P* traveltime difference.

4. Results

In this section, we describe the results in terms of which phases are identifiable in different portions of the study area and how their timing relates to the plate boundary and velocity models. Usually only one type of converted phase is observable at each onshore station, but both SP and Ps phases can be observed at the same OBS station. To discuss these results, we divide the onshore stations into four groups based on which type of converted phase is observed and other common features in the waveforms. In the main text, we show results for three of the onshore groups. Similar discussions of the remaining onshore group and the offshore stations can be found in the supplementary material.

4.1. Northern onshore stations with SP Phases

Stations JCC and CM01 A in the northernmost part of the array show large amplitude arrivals near the SP arrival time predicted by the Slab1.0 model (Figure 5). Ray tracing estimates the location of the SP conversion points to lie just offshore at depths between 10 and 15 km. We select events with large amplitude SP phases (red traces) on each station and apply the beamforming method to those wavelets. The beamforming

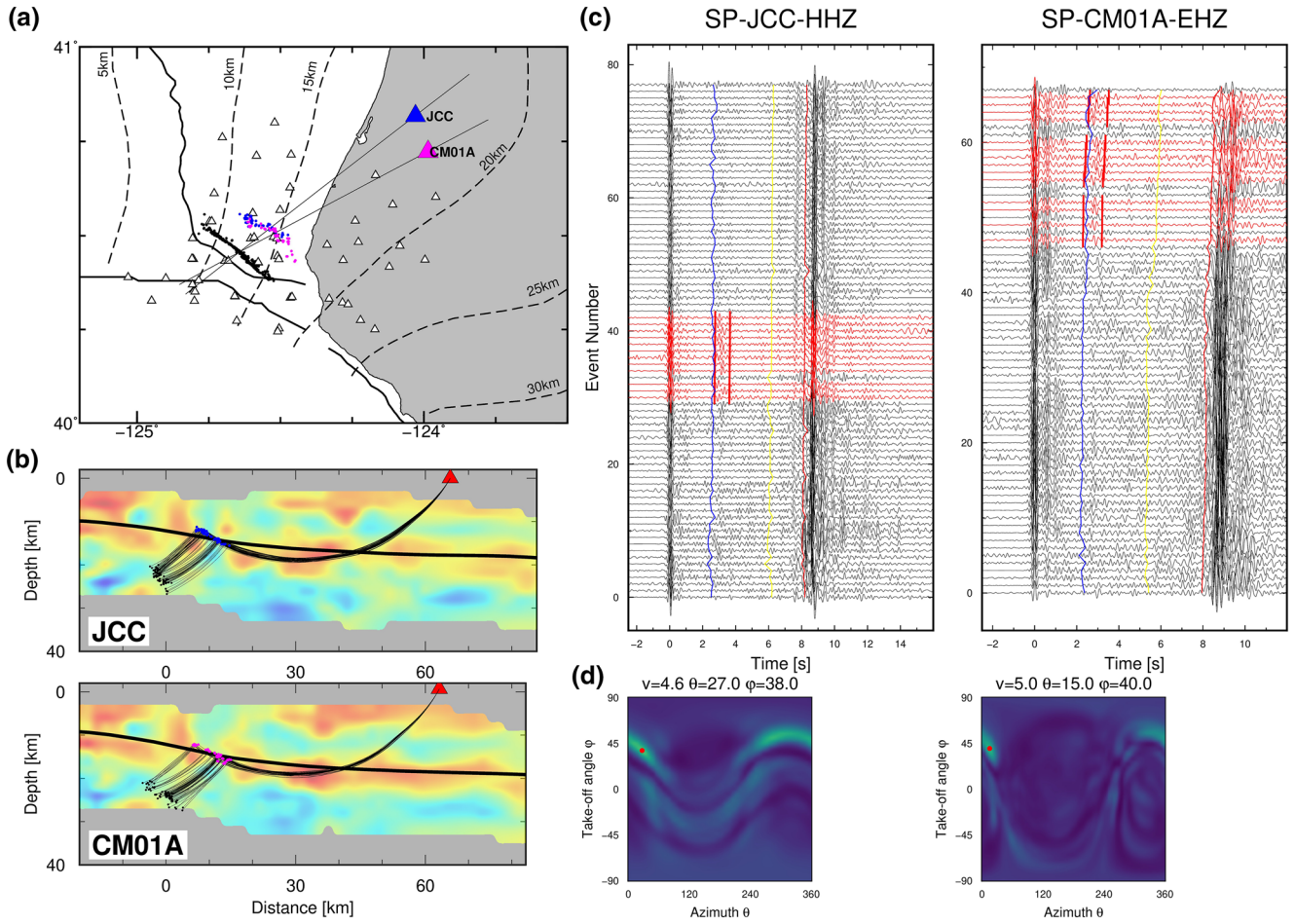

Figure 5. SP (reflection refraction type) converted phases at stations in the north. (a) Map view of the locations of the earthquakes (black dots), SP conversion points (magenta dots), the stations (triangles), and the cross sections shown in (b) going through the center of the M-fault events and stations JCC and CM01 A. (b) SP phase raypaths from the M-fault events to stations JCC and CM01 A. The background colors denote the Vp/Vs model as in Figure 2. (c) Waveform sections of M-fault events on vertical component of stations JCC and CM01 A. The waveforms are aligned by *P* wave and are sorted by *S-P* traveltime difference. Waveforms used for beamforming are highlighted in red with the red bars denoting the time window used in the beamforming analysis. The blue curve denotes the predicted SP arrival time from conversion at the Slab1.0 model and the yellow curve denotes the predicted arrival time from a conversion at an interface 10 km shallower than the Slab1.0 model. (d) Beamforming results for selected converted phases at JCC (left) and CM01 A (right). The maximum intensity point is marked by the red dots and the corresponding velocity, azimuth, and takeoff angle are given in the title of the panel.

results indicate those phases leave the source region with an *S* wave velocity at azimuths consistent with the event-station azimuth. The takeoff angles, which are 38 and 40°, respectively, are consistent with the ray tracing in Figure 5b, which predicts upward takeoff angles at about this angle. Based on the agreement with the predicted arrival times and the beamforming results, we identify these phases as SP converted phases near the Slab1.0 model interface. The actual arrival times are slightly later than the predicted ones, which might indicate that the actual slab interface is 1–2 km shallower than the model. Comparing to the Vp/Vs cross section in Figure 5b, the SP conversion points appear to be close to the top of the high Vp/Vs zone.

4.2. Southern onshore stations with SP Arrivals

We group together five stations in the southern part of the array, CM09 A, B046, CM10 A, B932, and B047, because they show SP converted phases from the Slab1.0 model depth as well as several SP phases converted at shallower discontinuities. The two stations, CM09 A and B047, with the clearest SP converted phases are shown in Figure 6. On the waveform sections, clear large amplitude signals near the predicted arrival time are observed. Their raypaths are shown in Figure 6b. The SP conversion points on the Slab1.0 model would

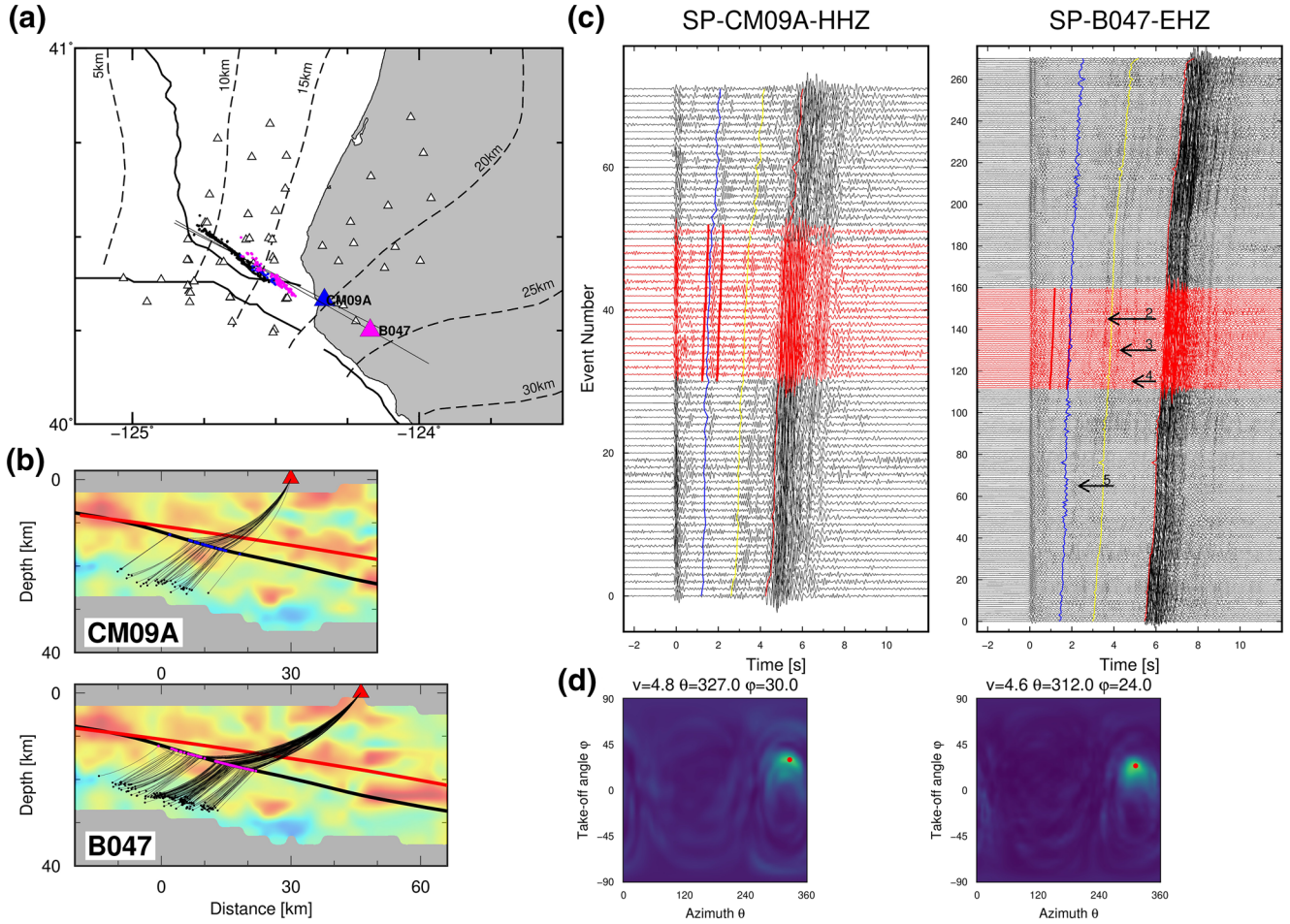

Figure 6. SP (mixed transmission and reflection refraction types) converted phases at stations in the south. (a) Map view of the locations of the earthquake (black dots), SP conversion points (magenta dots), the stations (triangles), and the cross sections shown in (b) going through the center of the M-fault events and stations CM09 A and B047. (b) SP phase raypaths from the M-fault events to stations CM09 A and B047. The colors denote the Vp/Vs model as in Figure 2. The bold black curves are the Slab1.0 model and the bold red curves are the Slab2 model. (c) Waveform sections of M-fault events on vertical component of stations CM09 A and B047. The waveforms are aligned by *P* wave and are sorted by *S-P* traveltime difference. Waveforms used for beamforming are highlighted in red with the red bars denoting the time window used in the beamforming analysis. The blue curve denotes the predicted SP arrival time for conversion at the Slab1.0 model interface and the yellow curve denotes the predicted SP arrival time from an interface 10 km shallower than the Slab1.0 model. Black arrows and the corresponding numbers denote converted phases from shallow velocity discontinuities that are analyzed in Figure 7. (d) Beamforming results for the converted phases in between the red lines at CM09 A (left) and B047 (right). The maximum intensity point is marked by the red dots and the corresponding velocity, azimuth, and takeoff angle are given in the title of the panel.

be between 12.5 and 17.5 km depth and located just offshore. We select events with large amplitudes and apply the beamforming method to those wavelets. The beamforming results indicate these phases leave the source with an *S* wave velocity at an azimuth consistent with the events-station azimuth. The takeoff angle estimates are 30 and 24°, respectively, which is consistent with the ray tracing Figure 6b. Based on the results from arrival time prediction and beamforming, we identify these phases as SP converted phases. The cross section in Figure 6b indicates that these SP conversion points likely convert near the bottom of the high Vp/Vs zone.

Several other coherent arrivals can be seen on the waveform section for station B047. They are labeled 2–5 in Figure 6c. Since their arrival times are later than the SP phase converted from the Slab1.0 interface, if they are also SP converted phases, they would have converted at shallower velocity discontinuities. We apply the beamforming method to these arrivals. The selected waveform for each potential shallow converted phase are shown in Figure 7c and their beamforming results are shown in Figure 7d. The results all indicate that these converted phases leave the source as *S* waves. Thus, we interpret these arrivals as SP converted phases.

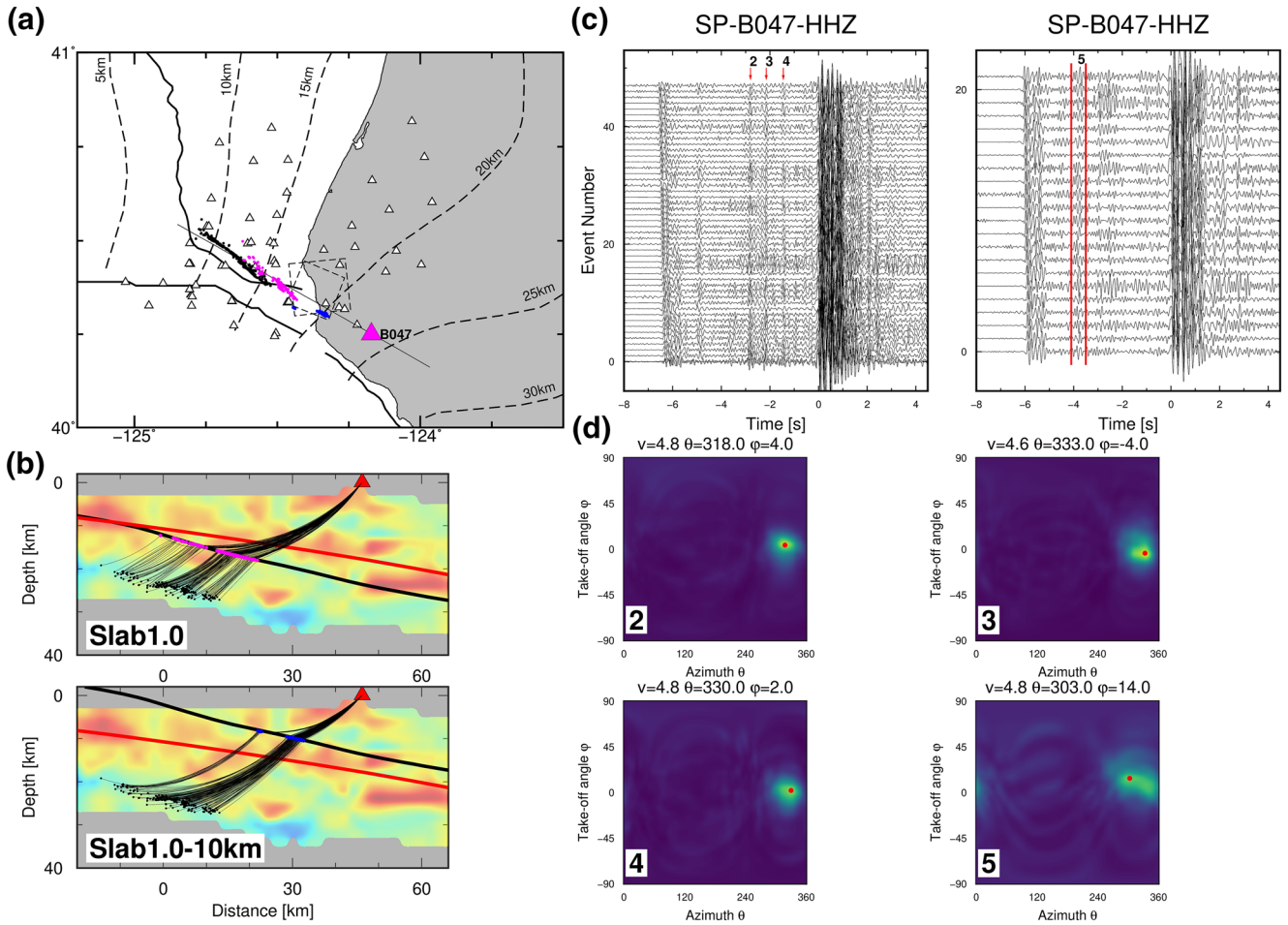

Figure 7. Shallow SP (transmission type) converted phases at station B047. (a) Map view of the locations of the earthquake (black dots), SP conversion points from Slab1.0 model interface (magenta dots) and Slab1.0 + 10 km model interface (blue dots), the station (triangle), the cross sections shown in (b) going through the center of the M-fault and station B047, and the rupture area of the 1992 Cape Mendocino earthquake from Murray et al. (1996). (b) SP phase raypaths from the M-fault events to station B047 for Slab1.0 and Slab1.0 + 10 km models. The background colors denote the Vp/Vs model as in Figure 2. The bold black curves are the Slab1.0 and Slab1.0 + 10 m models in the upper and lower panel, respectively. The bold red curves are the Slab2 model. (c) Waveform sections of M-fault events with clear shallow SP converted phases on vertical component of station B047. They are denoted by the same number as in Figure 6c. The waveforms are aligned by S wave and are sorted by *S-P* traveltime difference. (d) Beamforming results for the shallow SP converted phases at B047. The maximum intensity point is marked by the red dots and the corresponding velocity, azimuth, and takeoff angle are given in the title of the panel.

In Figures 7a and 7b, we plot the location of the conversion points and raypaths for both the Slab1.0 and the Slab1.0 + 10 km models. The SP 2–4 phases arrive near the predicted arrival time from the Slab1.0 –10 km model. The corresponding conversion points are at around 10 km depth onshore. The azimuth estimates are consistent with the station-events azimuth. The raypaths for the Slab1.0 − 10 km model have smaller take-off angles for the same events than the Slab1.0 model, which is consistent with the takeoff angle estimates from beamforming. Comparing with the Vp/Vs model, they are likely from the top of the high Vp/Vs layer (SP2) and other shallow geological boundaries within the overriding continental crust (SP3 and SP4). The SP3 and SP4 phases convert at interfaces more than 10 km shallower than the Slab1.0 model and these are likely in the vicinity of the 1992 Petrolia earthquake's fault plane which lies within the overriding plate (Guo et al., 2018; Murray et al., 1996). For SP5 phase, the arrival time is slightly after the predicted arrival time from the Slab1.0 model indicating it comes from an interface that is a few km shallower. We are not sure what the geologic interpretation of this interface is but it likely lies within the subducted plate. The takeoff azimuth of SP5 phase is somewhat offset from phases 1–4 but we cannot rule out that they are identical due to the higher uncertainty in the phase 5 results.

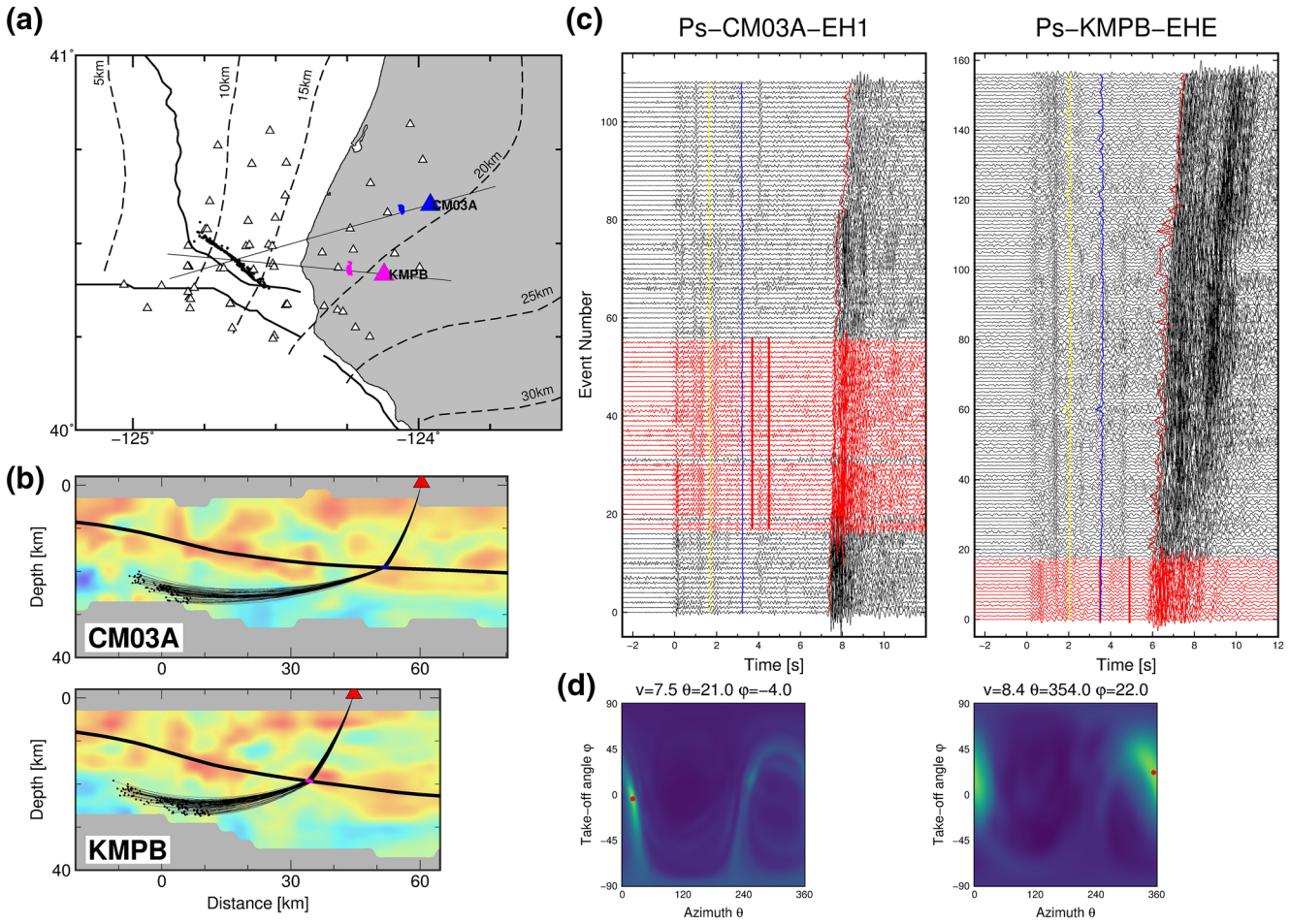

Figure 8. Ps converted phases at stations in the east. (a) Map view of the locations of the earthquake (black dots), Ps conversion points (magenta dots), the stations (triangles), and the of cross sections shown in (b) going through the center of the M-fault events to stations CM03 A and KMPB. (b) Ps phase raypaths from the M-fault events to stations CM03 A and KMPB. The background colors denote the Vp/Vs model as in Figure 2. (c) Waveform sections of M-fault events on horizontal components of station CM03 A and KMPB. The waveforms are aligned by P wave and are sorted by *S-P* traveltime difference. Waveforms used for beamforming are highlighted in red with the red bars denoting the time window used in the beamforming analysis. The blue curve denotes the predicted Ps arrival time for conversion at the Slab1.0 model interface and the yellow curve denotes the predicted Ps arrival time from an interface 10 km shallower than the Slab1.0 model. (d) Beamforming results for selected converted phases at CM03 A (left) and KMPB (right). The maximum intensity point is marked by the red dots and the corresponding velocity, azimuth, and takeoff angle are given in the title of the panel.

4.3. Eastern onshore stations with Ps Arrivals

Four stations, CM03 A, CM07 A, KMPB, and B045, in the eastern part of the study area are grouped together owing to clear Ps converted phases from below the depth of the Slab1.0 model. The two stations with the clearest Ps converted phases, CM03 A and KMPB, are shown in Figure 8. The locations of the Ps conversion points on the interface model would be between 17.5 and 20 km depth and just onshore (Figure 8b). On the waveform sections, there are clear signals about 1 s after the predicted arrival time on both stations. We select events with large amplitude Ps phases and apply the beamforming method to those wavelets. The beamforming results indicate that those phases leaving the source with a *P* wave velocity, and the azimuth estimates are consistent with the event-station azimuths. The estimated takeoff angle for CM03 A, −4°, is consistent with the Ps ray tracing Figure 8b. The takeoff angle estimated for KMPB, 22°, is slightly larger than raytracing results. The beamforming peak is more diffuse than many examples indicating a relative larger error in the takeoff angle estimates. Based on the results from arrival time prediction and beamforming, we identify these phases as Ps converted phases. Given that they arrive a full second later than the predicted arrival time and comparing to the cross section in Figure 8b, these Ps conversion points are likely from the bottom of the high Vp/Vs zone.

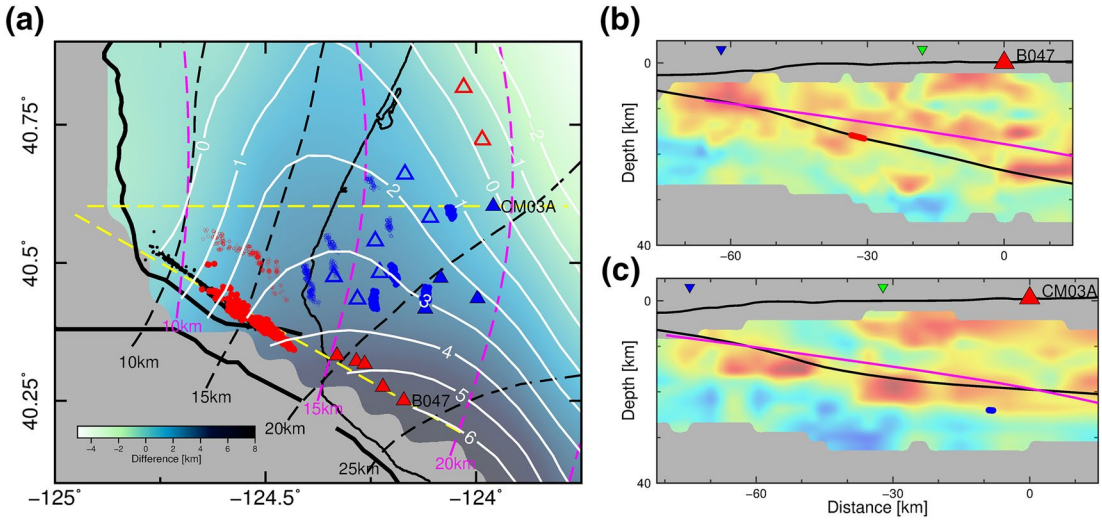

Figure 9. Comparison between the Slab1.0 and Slab2 models. (a) Map view of the difference in interface depth between the models. Positive values indicate where Slab1.0 is deeper than Slab2. Black dashed lines denote depth contours from the Slab1.0 model. Magenta dashed lines denote the depth contours from the Slab2 model. Yellow dashed lines are the two cross sections shown in (b) and (c). Red solid circles and red solid triangles are the SP conversion points from the oceanic Moho and the stations where these phases are observed. Red open circles and red open triangles are the P conversion points from the top of the oceanic crust and the stations where these phases are observed. Blue solid circles and blue solid triangles are the Ps conversion points from the oceanic Moho and the stations where these phases are observed. Blue empty circles and blue empty triangles are the Ps conversion points from the top of the oceanic crust and the stations where these phases are observed. (b) Cross section through station B047. The background colors denote the Vp/Vs model as in Figure 2. The green and blue inverse triangles indicate the point where the cross section intersects with the coastline and deformation front. Black and magenta lines are the slab geometry from Slab1.0 and Slab2 models, respectively. Red solid circles are the locations of the SP conversion points from the events used for beamforming analysis in Figure 6 at station B047. (c) Cross section going through station CM03 A. The blue solid circles are the locations of the Ps conversion points from the events used form beamforming analysis in Figure 8 at station CM03 A. Other symbols are the same as in (b).

5. Discussion

5.1. Implications for Slab Geometry

Specifying the geometry of the subduction interface is important for the estimation of ground motion in future large earthquakes and for geodetic studies that estimate the distribution of interseismic locking. Here we compare our estimated Ps and SP conversion depths with the Slab1.0 model (McCrory et al., 2012), the Slab2 model (Hayes et al., 2018) and the imaging results from the 93 to 94 Mendocino active source seismic experiments (Tréhu & Group, 1995). The Slab1.0 model is widely used in studying this part of the Cascadia subduction zone and it contains considerable structure that was derived primarily from earthquake relocations as well as the active source results. In the discussions below, all depth ranges are given in km below sea level and we assume the plate interface corresponds to a sharp discontinuity near the top of the high Vp/Vs zone. It is possible that the actual plate interface lies slightly below the top of the high Vp/Vs zone, but that fine scale structure is beyond our resolution.

Offshore, near the deformation front, the Slab1.0 model predicts that the plate interface is at about 7–8 km depth and the plate interface in the Slab2 model is about 1 km deeper (Figure 9). Using multichannel seismic data, Gulick et al. (1998) imaged the sediment and crustal structure near the deformation front. Their results for Line 6 (Figure 3 in Gulick et al. (1998)), which intersects the deformation front at about 40.7°N, indicates that the depth of the top of the oceanic crust is at 5–6 km, which is 1–3 km shallower than the Slab1.0 model.

Our measurements of the traveltime differences between the Ps and P arrivals or between the SP and S arrivals from the OBS records place constraints on the location of the plate boundary near the deformation front, but they require additional information about P and S velocities in the shallow sediments which are not resolved by the tomographic model. Let H be the thickness of the sediment layer with homogeneous velocities v_s and v_p and assuming vertically traveling waves, the traveltime difference Δt between Ps and P or between SP and S wave are both given by

$$\Delta t = \frac{H}{v_s} - \frac{H}{v_p} \tag{9}$$

$$= t^P (r - 1) \tag{10}$$

where r is the Vp/Vs ratio and t^P is the one-way P wave traveltime in the sediments. We take stations FS13D and FS41D as example stations (Figure s7) and estimate t^P using the migration image from Figure 8 of Gulick et al. (1998). In that figure, the two-way traveltime (TWT) from the sea surface to the top of the oceanic crust is about 5.5 s along the entire migrated section. FS13D is located just seaward of the deformation front at a water depth of 2.3 km and FS41D is located on the continental slope about 10 km landward of the deformation front at a depth of 1.1 km. Given the water depth of stations and the acoustic velocity in the water (1.5 km/s), the P wave TWT inside the sediment layer would be about 2.4 and 4.0 s for FS13D and FS41D, corresponding to t^P values of 1.2 and 2.0 s, respectively. Since the traveltime differences between Ps and P or between SP and S are around 2.5 s for both stations (Figure s6), we estimate the average Vp/Vs ratio of the underlaying sediment is about 3.1 for FS13D and 2.3 for FS41D. If we further assume that the average P wave velocity inside the sediment to be in the range from 2.5 to 3.5 km/s (Gulick et al., 1998), the locations of the plate interface are at about 5.3–6.5 and 6.1–8.1 km at FS13D and FS41D. However, the plate interface is at about 9 km beneath the two stations from the Slab1.0 model. Near the trench, we prefer the active source imaging results. The Slab1.0 model appears to overestimate the depth of the plate interface for by 1–4 km.

Offshore, at the location of the SP conversion points observed by stations JCC and CM01 A, the Slab1.0 model is 1–2 km deeper than the Slab2 model (Figure 9). From our converted phase observations, the arrival time of the SP converted phases on stations CM01 A and JCC from the top of the crust are slightly later than the predicted arrival time from the Slab1.0 model, which indicates a 1–2 km shallower interface that corresponds to the top of the high Vp/Vs zone. Thus, just offshore, the SP arrival times are more consistent with the Slab2 model.

At the coastline and just onshore, the Slab1.0 model predicts the plate interface is at about 17 km depth (Figure 1), while Beaudoin et al. (1994) imaged the top of the Gorda crust at about 13–14 km. The Slab2 model is about 2–4 km shallower than the Slab1.0 model (Figure 9) near the coastline, which is more consistent with the active source result. Ps arrivals at KCT and CM06 A (Figure s5) convert near the coast and arrive close to the Slab1.0 model predicted arrival time, indicating there is an interface close to the Slab1.0 model. However, the converted phases represented by the open blue triangles in Figure 9 (including KCT and CM06 A) are less clear than other stations and multiple Ps phases are observed between the direct P and S phases (Figure s5c), which indicates a complex velocity structures near the coast. The main Ps arrival at KCT, the Vp/Vs model, and the active source results favor an interface 2–3 km shallower than Slab1.0 and consistent with Slab2.

Ps conversions at stations KMPB and CM03 A allow us to investigate the slab interface at 20–40 km inland from the coast from 40.4°N to 40.7° N. These stations are near the 20 km contour of the Slab1.0 model and the model lies near the top of the high Vp/Vs zone. Both stations show very strong conversions from the subducted Moho that lie 3–5 km deeper than the Slab1.0 Model. The top of the subducted crust is less clear at these stations but perhaps small coherent arrivals are visible on CM03 A (Figure 8 and s9). Given that the thickness of oceanic crust is about 6–8 km, the plate interface likely lies about 1–2 km shallower than the Slab1.0 model in this region based on the Vp/Vs model and the Moho conversions at CM03 A. At the location of the Ps conversion points for stations KMPB and CM03 A, the Slab2 model is 3 and 1 km shallower than Slab1.0 model (Figure 9). Thus, we prefer the Slab2 model at those locations.

South of 40.5° N the Slab1.0 model contours at depths of 20–30 km is highly curved and indicate that the slab dip is significantly steeper from 15 to 25 km depth in the 40.3°N to 40.5°N latitude range. Stations B047 and CM09 A are located in this area and show very clear SP conversions from the Moho of the subducted slab that arrive at or just before the time predicted for the Slab1.0 model. The Slab2 model is 2–4 km shallower than the Slab1.0 model at the location of these SP conversion points (Figure 9). Thus, the Slab1.0 model is likely too deep by an amount corresponding to the crustal thickness. This inference is corroborated

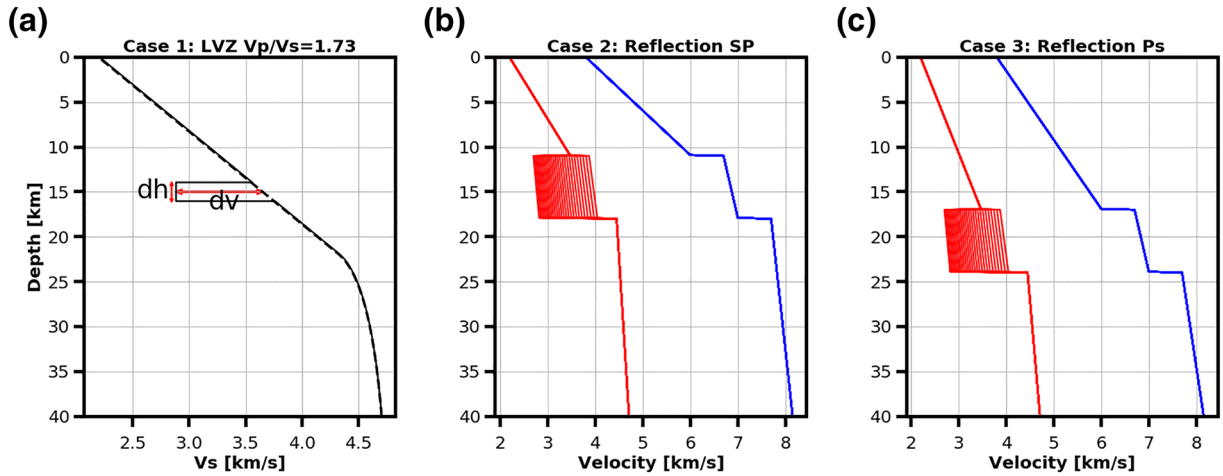

Figure 10. Velocity models for calculating synthetic seismograms. (a) Case 1, *S* wave LVZ models. A low velocity layer centered at 15 km depth with various thickness (dh) and velocity reduction (dv). The Vp/Vs in the entire model is fixed at 1.73. (b) and (c) Cases 2 and 3, velocity models based on Beaudoin et al. (1994). Blue and red lines denote the *P* and *S* wave velocity models respectively. *P* wave velocity increases linearly in depth with two steps representing the top and bottom of the subducted oceanic crust. Outside the subducted crust, the Vp/Vs ratio is 1.73. Inside the subducted crust, the Vp/Vs ratio varies from 1.73 to 2.51 for different models. Density (ρ) models follow the default relation in FK software, where $\rho = 0.77 + 0.32 * \text{Vp}$.

by the Vp/Vs model which shows the interface model lying at the base of the high Vp/Vs zone. The high Vp/Vs values near station B047 may also reflect the Mendocino Transform Fault's damage zone. Both B047 and CM09 As show multiple clear arrivals from shallower depths that are roughly 8–12 km above the interface model and correspond to the top of the high Vp/Vs zone. Thus, we prefer a model where the slab interface is roughly 6–8 km shallower than the Slab1.0 model and about 2 km shallower than the Slab2 model in the 40.3°N to 40.5°N latitude range and find no evidence for the considerable steepening of slab dip shown at the southernmost end of the Slab1.0 model.

5.2. Estimation of velocity Contrast

To further investigate the material properties of the high Vp/Vs zone, we compare measurements of the amplitude ratios Ps/P and SP/P made on both the actual data and on synthetic seismograms for simple models of the subducted crust (Figure 10). We measured the amplitude ratio of the Ps or SP converted phases to the direct *P* wave using the three component velocity seismograms filtered in the same filter bands used in section 3. The maximum amplitude of the Ps converted phase was measured as the maximum vector length on the two horizontal components. The maximum amplitudes of the SP converted phase were measured on the vertical component. The maximum amplitudes of the *P* wave were measured as the maximum vector length on three components. The distribution of the amplitude ratios for each station are shown in Figures 11c. The values typically range from 0.1 to 1.0 with many observations in the 0.2–0.5 range indicating strong velocity contrasts. We note that these measurements were made on the clear arrivals used for beamforming in section 5. While they are from representative parts of the waveform sections for each station, they likely represent the locations where the velocity contrasts are among the strongest.

We first calculated synthetic seismograms using an averaged 1D velocity model derived from the tomographic model but with a low velocity layer of variable thickness inserted and centered at 15 km depth, which we term case 1 (Figure 10a). The frequency-wavenumber summation method (Zhu & Rivera, 2002) is used to calculated synthetic seismograms. The thickness of the low velocity layer was varied from 100 to 4,000 m and the velocity reduction inside this layer relative to the original velocity at 15 km depth varies from 1% to 30%. We fixed the focal mechanism of the sources to be 128°/90°/180° in strike, dip and rake (convention in Aki and Richards (2002)). The focal mechanism is based on the alignment of earthquake hypocenters and the focal mechanism results from Li et al. (2018). Synthetic waveforms were calculated for stations CM09 A, B047, CM01 A, KMPB, and CM03 A. The distance and azimuth settings are the averaged

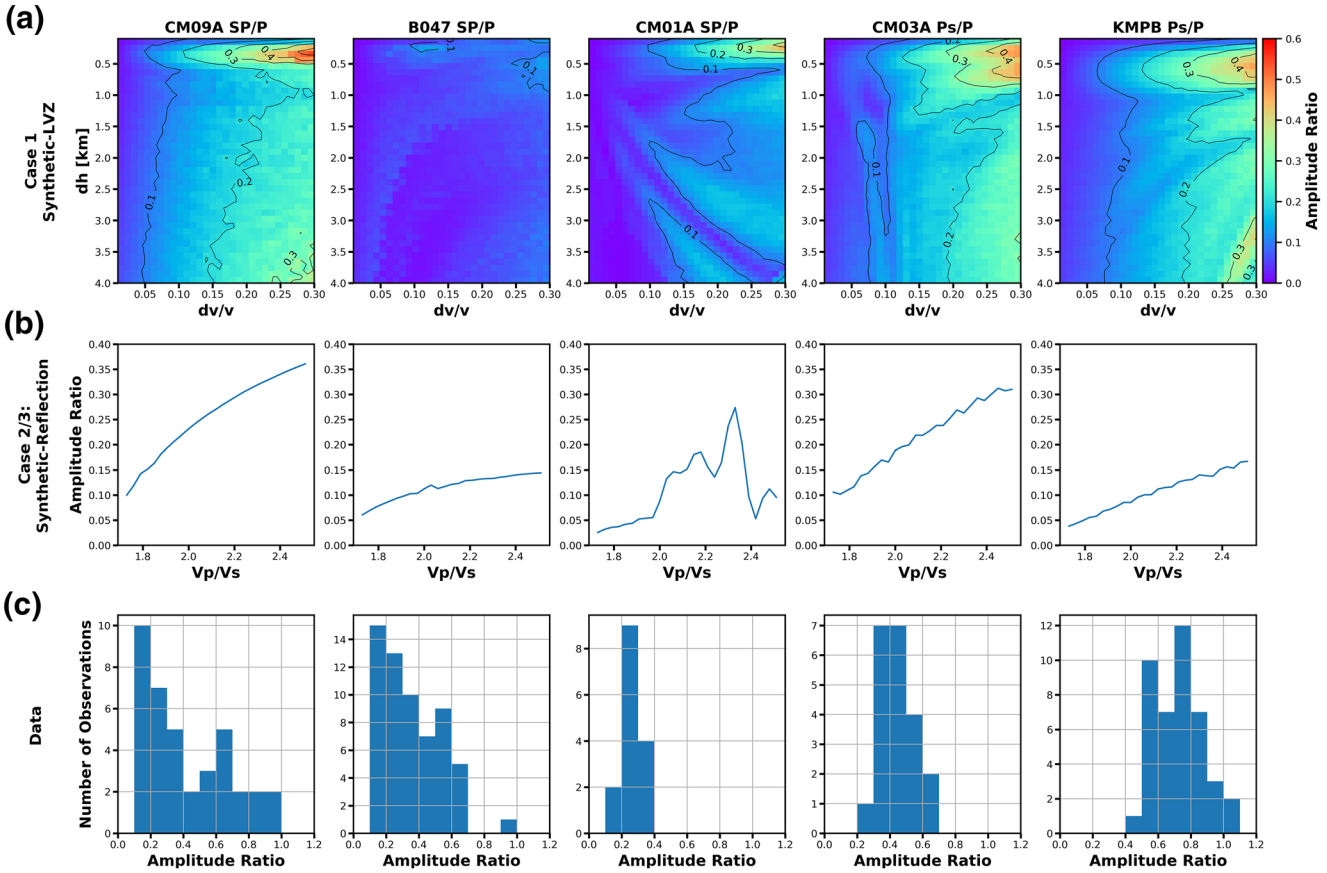

Figure 11. Amplitude ratio measurements from synthetic seismograms and real data. Each station is shown as three panels in its own vertical column. (a) SP/P and Ps/P amplitude ratios for the Case 1 LVZ models in Figure 10 as a function of the dv/v value and thickness of the LVZ. (b) SP/P and Ps/P amplitude ratio for the Cases 2 and 3 reflection models in Figure 10. Case 2 is used for the stations with SP observations and Case 3 for the stations with Ps observations. (c) Frequency distribution of the amplitude ratio of the converted phases to the direct P phases measured on real data using the same subset of seismograms that was utilized for beamforming in section 4.

distance and azimuth from each station to the earthquakes used for beamforming in section 5 and are listed in Table S2.

We also calculated synthetics for 1D velocity models that match the *P* wave velocity profile from the Beaudoin et al. (1994) refraction model. Importantly this profile does not contain a low velocity zone in the subducted crust for *P* wave velocities but is primarily characterized by discontinuities at the top and bottom of the subducted crust. The top of the crust corresponds to a jump from 6.0 to 6.7 km/s and the bottom of the crust (Moho) corresponds to a jump from 7.0 to 7.7 km/s. We developed synthetics for two versions of this model. In Case 2, the crust is between 11 and 18 km, and in Case 3 it is at 17–24. Case 2 corresponds to our offshore SP conversions and Case 3 corresponds to our onshore Ps conversions. For both Cases 2 and 3, we varied the Vp/Vs ratio from 1.73 to 2.5 inside the oceanic crust, while keeping the Vp/Vs equal to 1.73 outside the crust. Cases 2 and 3 are meant to provide a simple representation that combines the features of the Beaudoin et al. (1994) and the Guo et al. (2018) tomographic models.

The Case 1 amplitude ratio measurements for stations CM09 A, CM01 A, CM03 A, and KMPB show the expected overall patterns, where the amplitude ratio increases as velocity reduction increases. The largest ratio appears near the top right part of each plot and corresponds to cases with constructive interference between the two converted phases generated at the top and bottom of the low velocity layer. For station B047, the synthetic results are more complicated. The epicentral distance of station B047, about 45 km, corresponds to a range where the SP phases are expected to refract along the bottom interface of the LVZ which causes complex waveforms (1B in Figure s8). The amplitude of such phases are not simple measures

of the transmission coefficient corresponding to the velocity contrast at the bottom of the LVZ, and we do not interpret the B047 amplitudes.

The Case 2 and 3 amplitude ratio measurements for stations CM09 A, B047, CM03 A, and KMPB show that the amplitude ratio increases as the Vp/Vs ratio inside the oceanic crust layer increases as expected. For station CM01 A, the sudden increase in amplitude ratio between 1.9 and 2.4 in Vp/Vs values is due to the interference of the Ps arrival. But without the contamination of Ps phases, the amplitude ratios are still small, likely below 0.1.

We seek a representative estimate of the velocity contrast across the top and bottom boundaries of the high Vp/Vs zone by comparing the real and synthetic amplitude ratios. However, even though the amplitude ratios are from events in a compact cluster that generates similar waveforms, the observed amplitude ratios are scattered over a certain range. Similarly, the synthetics are calculated for a very simplified velocity model that is not a complete representation of the true Earth. Thus, we focus on the first order implications of the amplitude ratios and recognize that effects like focal mechanism variations as well as local variations in the both the strength and dip of the discontinuities can lead to the significant level of variability in amplitude ratio (factor of 2+) that is observed for any particular station-phase pair.

In general, for stations CM09 A, CM01 A, CM03 A, and KMPB, the observed amplitude ratios are larger than can be replicated by the simple synthetics. In particular, there are no models for which a Vp/Vs ratio around 1.7–1.8 could satisfy the observed amplitude ratios. For models in Cases 2 and 3, once the Vp/Vs ratio exceeds 2.0, the subducted crust becomes a low velocity zone. Models in the range $2.0 \leq Vp/Vs \leq 2.5$ produce amplitude ratios that overlap the observations but do not capture the full range of the observations. Thus, we do not favor a specific value for the Vp/Vs ratio in the subducted crust recognizing that our models are highly simplified. However, given the large observed amplitude ratios we favor a Vp/Vs value in ≥ 2.0. Thus, the plate boundary fault is likely contained within a LVZ, at least for shear-wave velocity.

A LVZ would be expected to generate converted phases from both its top and bottom interfaces. In general, our observations agree with this in that for certain clusters of stations we clearly see either the top or the bottom of the high Vp/Vs layer as a sharp velocity contrast. We have relatively few cases where the seismograms are simple enough to interpret distinct arrivals on the same seismogram as coming from the top and bottom of the high Vp/Vs layer. Perhaps the multiple converted phases on B047 is the best case as these are widely separated in time. Station CM03 A presents an interesting case that directly constrains the properties of the interseismically locked zone in that while the Moho Ps conversion is the largest phase, coherent phases are observed from shallower depths as well. Figure s9 shows an expanded view of a few of these seismograms compared to synthetics. The conversion from the subducted Moho is about twice as large as the phase which arrives immediately before it. The two Ps phases are separated by about 1.1 s and may have opposite polarity, though that is difficult to assess. Figure s9 shows radial component synthetics for various case 3 models. The synthetics demonstrate that the amplitude of the shallower phase is minimized for a Vp/Vs of about 2.0. For Vp/Vs larger than 2.0, the LVZ creates two phases with opposite polarities that are separated by 1.3–1.5 s with varying amplitude ratios. Again, we do not attempt to specify a specific Vp/Vs ratio from the simplified synthetics, but the CM03 A waveforms are consistent with the seismogenic zone being characterized by a ~5 km thick LVZ with a $Vp/Vs \geq 2$.

The inference of a likely low velocity zone in Versus at seismogenic depths likely implies elevated fluid content in the vicinity of the locked zone. The subducted oceanic crustal basalt of Gorda plate is likely to be metamorphosed to greenschist facies at depths of 10–20 km, which has a Vp/Vs value of ~1.76 (Christensen, 1996). Thus, the elevated Vp/Vs values in Models two and three that are consistent with the converted phase amplitudes likely indicate the existence of significant fluid-filled porosity in the subducted melange and oceanic crust. To reach Vp/Vs values in excess of ~1.85 would likely correspond to fluid-filled porosities in excess of ~3% (assuming 20–50 MPa effective normal stress) (Peacock et al., 2011; Pimienta et al., 2018). While the exact amount of fluid-filled porosity is difficult for us to interpret owing to the variety of factors that affect the converted phase amplitudes, our results are consistent with the interpretation of the 10–20 km depth range as being dominated by brittle deformation that produces significant porosity which is maintained throughout the interseismic peirod.

5.3. Single station Variability in Converted Phase Amplitudes

The observed SP/P or Ps/P amplitude ratios at a single station often show a range over a factor of 3 (or more) even for the similar clusters of events that we used for beamforming. Moreover, the clusters that we selected are some of the clearest examples with other portions of an individual record section showing less systematic converted phase arrivals. This variability is surprising, particularly for phases associated with the Moho of the subducted plate whose conversion points are tightly clustered in a few km areas such as for the KMPB Ps arrivals from the bottom of the high Vp/Vs zone (Figure 8). In this section, we explore some possible causes of this variability.

While we have only used earthquakes from a linear vertical, strike-slip fault segment for this study to isolate structural effects on the waveforms, focal mechanism variability within the source arrays may still contribute to SP or Ps amplitude variability. Moreover, the ~30 km length of the M-fault used to make our record sections leads to a natural variation in the takeoff angles of the direct and converted phases across the record section. To explore how these combined effects on the initial excitation of the *P* or *S* waves leaving the source are reflected in the converted phase amplitude ratios, we use the S/P amplitude ratio as a proxy for focal mechanism and takeoff angle changes along the profiles.

To examine if the large variability in the amplitude ratio measurements could be a result of variations in focal mechanisms, we run simulations corresponding to models in Figures 11a by randomly perturbing the focal mechanism. The results are shown in Figure s10. We fix the thickness of the LVZ to be 4 km and select three shear-wave velocity reductions: 10%, 20%, and 30%. The strike angles are perturbed in the range of ±10°. The dip angles are perturbed in the ranges of 0–5°, 0–10°, and 0–20°. The rake angles are perturbed in the ranges of ±5°, ±10°, and ±20°. We draw 500 random selections under uniform distribution for strike, dip and rake. The amplitude ratio variabilities are different for each station. In general, the focal mechanism variations do not cause a large enough variability in amplitude ratios to obscure the different levels of velocity reduction. Larger perturbation range results in larger variability in amplitude ratio measurements. SP phases have larger amplitude ratio variability than Ps phases. CM09 A and B047 have the largest amplitude ratio variability, which we attribute to the near nodal plane orientation for P wave. For station CM09 A, B047 and CM01 A, focal mechanism variations could account for a factor of 2–3 in the amplitude ratio variability. For station CM03 A and KMPB, focal mechanism variations could account for a factor of <1.5 in the amplitude ratio variability.

Figures s11–s13 show how the SP/P and Ps/P amplitude ratios vary within clusters of relatively similar earthquakes. Figure s11 shows about a factor of two variation in the SP/P amplitude ratio at CM01 A across a cluster of 11 events with very similar waveforms (a subset of the beamforming dataset in section 3). Despite having extremely similar *P* waveforms, there is considerable variation in both the S/P and SP/P amplitude ratios. Figure s12 shows common events recorded by stations CM09 A and B047 and by stations CM03 A and KMPB. The SP/P amplitude ratio relation between CM09 A and B047 shows a positive correlation while the Ps/P amplitude ratio relation between CM03 A and KMPB shows a negative correlation indicating relatively systematic trends despite the small size of the earthquake cluster. Lastly, Figure s13 compares the converted phase and direct wave amplitude ratios, which are expected to be correlated based on standard formulas for conversion and transmission coefficients (Aki & Richards, 2002). The strong correlation at stations like CM09 A indicates that much of the variability seen in the measurements in Figure 11 results from variations in the initial excitation as the *P* and *S* waves leave the source region.

Collectively these figures indicate that much of the variation in the converted phase amplitudes on an individual record section results from the natural variability in the initial excitation of the direct and converted waves as they leave the source region of an individual earthquake somewhere along the M-fault. Some of this variability in excitation may be due to focal mechanism variability but it may also result from the variations in takeoff angles between the different locations along the fault. Additionally, any small scale variations in velocity contrasts across the various discontinuities will also contribute the variability seen in a particular record section. Special care should be given in interpreting the Ps/P ratios because variation in shear-wave speeds near the station can cause local amplification of the shear-wave amplitude that is not related to the actual conversion at greater depth. For instance, at the OBS stations like FS13D, the Ps phase are extremely clear, which likely reflects the low shear-wave speeds of the near seafloor sediments.

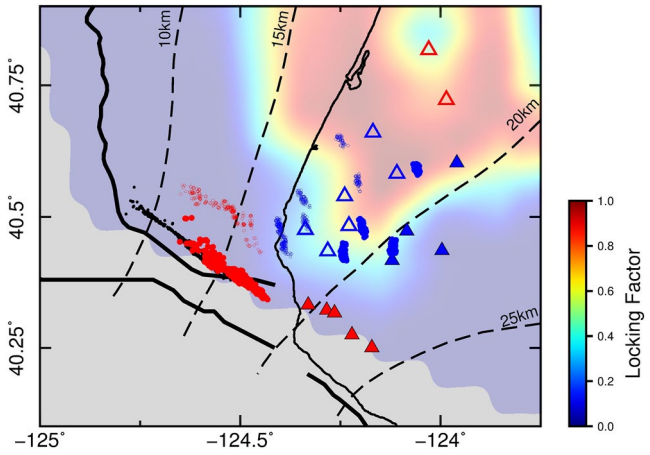

Figure 12. Mapview of conversion points on the Slab1.0 interface from onshore stations. Red solid circles and red solid triangles are the SP conversion points from the oceanic Moho and the stations where these phases are observed. Red open circles and red open triangles are the SP conversion points from the top of the oceanic crust and the stations where these phases are observed. Blue solid circles and blue solid triangles are the Ps conversion points from the oceanic Moho and the stations where these phases are observed. Blue empty circles and blue empty triangles are the Ps conversion points from the top of the oceanic crust and the stations where these phases are observed. Background colors represent the interseismic plate locking model from Pollitz and Evans (2017) ranging from freely slipping (locking factor 0) to fully locked (locking factor 1).

Additionally, there are many examples where the converted phases from either the top or bottom of the subducted crust are strong and easily established but the corresponding arrival from the other interface is not easily identified. For instance, the Sp phases in Figure 5 at JCC and CM01 A are very consistent with conversions from near the top of the subducted crust, but no similar Moho converted phase is observed. Moreover, some converted phases are only clearly visible at a subset of earthquakes and not in ones located a few km away on the same fault (also, see Figure 5). Both types of observations imply rapid spatial variations in the strength of the discontinuity.

5.4. Spatial Variations in the Converted Phases Observations

We summarize our observations from the onshore stations in Figure 12. SP converted phases are primarily observed by stations in the north and south groups and the corresponding conversion points are located just offshore. The SP phases observed at stations in the northern group convert near the top of the LVZ, while the largest SP phases observed at the southern group of stations convert near the bottom of the LVZ but shallower interfaces also generate SP phases. The Ps conversion points are located onshore between 15 and 20 km depth. Near the coast the Ps converted phases are from the top of the LVZ, while farther onshore the clearest Ps converted phases are from the bottom of the LVZ. The amplitudes of the Ps converted phases from the top of the LVZ near the coast are typically small, while the amplitude of the Ps converted phases for the slab Moho near 20 km depth is typically much larger resulting in clearer phases on the seismogram. The variations in whether Ps or SP are most clearly observed may reflect the strike-slip radiation pattern.

Figure 12 compares the locations of the conversion points to the interseismic coupling model of Pollitz and Evans (2017). The coupling model shows one of its strongest patches of interseismic locking in southern Cascadia, which overlaps our study area. Many of our conversion points are located offshore where there is no geodetic data and the coupling model is unresolved. Additionally, the southern boundary of this coupling patch is very dependent on how the modeling deals with the complicated geometry at the southern end of the subduction zone and the interseismic coupling on the transform boundaries. Thus, the decrease in coupling in the southernmost part of our study area is potentially unreliable and we do not seek to interpret it. The primary inferences we can make related to plate coupling are that the Ps conversions from the Moho in the highly coupled zone are some of our brightest phases (e.g., Ps at CM03 A and KMPB in Figure 8). We also observe converted phases from the top of the high Vp/Vs zone within the region of nearly full interseismic locking (Figure s9). Thus, in agreement with the Vp/Vs tomographic model, the converted phases support the inference that the interseismically locked zone is also a region of reduced seismic velocities and likely elevated porosity and fluid content (Guo et al., 2018).

6. Conclusions

The Cascadia Initiative onshore-offshore experiment demonstrates the ability to use converted phases from earthquakes in the mantle of the downgoing plate to study the geometry and physical properties of the plate boundary zone as well as the spatial scales that such observations can be expected to vary over. The combination of the 3D raytracing and source side beamforming methods was sufficient to identify the type of converted phases and infer the location of the major velocity contrasts in our dataset. In general, converted phases are similar among stations spaced less than about 30 km apart because the conversion points are more closely spaced at depth. For a given station, the SP conversion points occur well updip of where the Ps conversion points occur. At larger separations, it can be difficult to identify similar phases between stations. At offshore stations the basalt to sediment interface provides the largest amplitude conversions while at onshore stations, the Moho of the subducted Gorda plate provides the clearest interface at many stations

while the top of the subducted crust provides the clearest interface at some stations. In both onshore and offshore stations there are often conversions from multiple interfaces including phases generated within the shallow crust of the overriding plate.

In general, the Slab2 model provides a description of the subducted plate morphology that is more consistent with our converted phase observations and is near the top of the high Vp/Vs zone of Guo et al. (2018). Using the Ps converted phases at OBS stations near the deformation front and comparing to available active source reflection profiles indicates that the plate interface should be 1–3 km shallower than the Slab1.0 model and 1–4 km shallower than the Slab2 model at the deformation front. Just offshore, SP converted phases observed at CM01 A and JCC indicate the top of the oceanic crust is likely about 2 km shallower than the Slab1.0 model and are consistent with Slab2 model. Near the coast and onshore, multiple Ps converted phases are observed at the stations in the middle of our study area. Slab2 is 2–4 km shallower than Slab1.0 model in this area and consistent with the Vp/Vs model. East of 124.25°W and north of 40.5°N, Ps phases indicate that the Slab1.0 model is 1–3 km to deep but are consistent with the Slab2 model. The largest discrepancy between the Slab1.0 and Slab2 models is onshore between 40.3°N and 40.5°N where the Slab1.0 model shows a considerable steepening. We find that the high Vp/Vs zone lies largely above the Slab1.0 model in this area and that based on SP conversions from the subducted Moho as well as the likely top of the subducted crust, the true interface depth is about 6–8 km shallower than the Slab1.0 model and about 2 km shallower than the Slab2 model.

We observe clear converted phases from both the top and bottom of the subducted crust in the seismogenic zone in regions where the interface is inferred to be locked during the interseismic period. To further investigate the material properties of the locked zone we compared the SP/P and Ps/P amplitude ratios to a series of simplified models via synthetic seismogram calculations. We find that it is difficult to recreate the observed range of amplitude ratios (0.1–0.8) using simple models of a low velocity zone with an ordinary Vp/Vs ratio and moderate amounts of velocity reduction (≤10%). We also tested a model similar to *P* wave refraction profile of Beaudoin et al. (1994), which contains 10% velocity increases at both the top and bottom of the oceanic crust. To recreate the full amplitude of the observed SP/P and Ps/S ratios from the top and bottom of the subducted crust it was necessary to impose a low velocity zone in the oceanic crust with a Vp/Vs ratio ≥2.0. The tested velocity models are highly simplified compared to the real earth and a variety of effects may contribute to the observed range of converted phase amplitudes. However, the observed amplitudes are most easily explained by a subducted crust that is a significant low velocity zone at least for S-waves. Improved imaging of the subducted crust and plate boundary zone could be achieved in this region by designing receiver arrays capable of resolving the energy that propagates within the subducted crust for much of its path.

Acknowledgments
This work is funded by National Science Foundation Award Numbers EAR-1520690. The offshore data used in this research were provided by instruments from the Ocean Bottom Seismograph Instrument Pool and the on land data are from the PASSCAL facility, Northern California Earthquake Data Center and Plate Boundary Observatory. The seismic data are archived at the Incorporated Research Institutions for Seismology (IRIS) Data Management Center (http://www.iris.edu) and Northern California Earthquake Data Center (https://ncedc.org). We thank OBSIP and PASSCAL technicians and volunteers who contributed to data collection. Work presented here would not have been possible without the tomographic models and earthquake locations from Hao Guo. We thank John Collins for suggesting the wavefield decomposition method for processing the OBS data. We also thank Anne Tréhu for the discussion of the results of the 93–94 Mendocino active source seismic experiments. We appreciate Erin Wirth's, Joan Gomberg's and Stephen Hickman's helpful comments and suggestions on an earlier version of this paper. We thank Editor Michael Bostock and two anonymous reviewers for their constructive comments on the manuscript.

References

Abers, G. A., MacKenzie, L. S., Rondenay, S., Zhang, Z., Wech, A. G., & Creager, K. C. (2009). Imaging the source region of Cascadia tremor and intermediate-depth earthquakes. *Geology*, *37*(12), 1119–1122. https://doi.org/10.1130/G30143A.1

Aki, K., & Richards, P. G. (2002). *Quantitative seismology* (2nd ed.). University Science Books.

Amundsen, L., & Reitan, A. (1995). Decomposition of multicomponent seafloor data into upgoing and downgoing P and S waves. *Geophysics*, *60*(2), 563–572. https://doi.org/10.1190/1.1443794

Atwater, B. F., Nelson, A. R., Clague, J. J., Carver, G. A., Yamaguchi, D. K., Bobrowsky, P. T., & Reinhart, M. A. (1995). Summary of coastal geologic evidence for past great earthquakes at the Cascadia subduction zone. *Earthquake Spectra*, *11*(1), 1–18. https://doi.org/10.1193/1.1585800

Audet, P., Bostock, M. G., Christensen, N. I., & Peacock, S. M. (2009). Seismic evidence for overpressured subducted oceanic crust and megathrust fault sealing. *Nature*, *457*, 76. https://doi.org/10.1038/nature07650

Audet, P., & Schaeffer, A. J. (2018). Fluid pressure and shear zone development over the locked to slow slip region in Cascadia. *Science Advances*, *4*(3), eaar2982. https://doi.org/10.1126/sciadv.aar2982

Beaudoin, B. C., Hole, J. A., Klemperer, S. L., & Tréhu, A. M. (1998). Location of the southern edge of the Gorda slab and evidence for an adjacent asthenospheric window: Results from seismic profiling and gravity. *Journal of Geophysical Research*, *103*(B12), 30101–30115. https://doi.org/10.1029/98JB02231

Beaudoin, B. C., Magee, M., & Benz, H. (1994). Crustal velocity structure north of the Mendocino Triple Junction. *Geophysical Research Letters*, *21*(21), 2319–2322. https://doi.org/10.1029/94GL02154

Bilek, S. L., & Lay, T. (1999). Rigidity variations with depth along interplate megathrust faults in subduction zones. *Nature*, *400*(6743), 443–446. https://doi.org/10.1038/22739

Bruhat, L., & Segall, P. (2016). Coupling on the northern Cascadia subduction zone from geodetic measurements and physics-based models. *Journal of Geophysical Research: Solid Earth*, *121*, 8297–8314. https://doi.org/10.1002/2016JB013267

Chen, X., & McGuire, J. J. (2016). Measuring earthquake source parameters in the Mendocino triple junction region using a dense OBS array: Implications for fault strength variations. *Earth and Planetary Science Letters*, *453*, 276–287. https://doi.org/10.1016/j.epsl.2016.08.022

Christensen, N. I. (1996). Poisson's ratio and crustal seismology. *Journal of Geophysical Research*, *101*(B2), 3139–3156. https://doi.org/10.1029/95JB03446

Eberhart-Phillips, D., & Reyners, M. (1999). Plate interface properties in the Northeast Hikurangi Subduction Zone, New Zealand, from converted seismic waves. *Geophysical Research Letters*, *26*(16), 2565–2568. https://doi.org/10.1029/1999GL900567

Evans, R. L., Wannamaker, P. E., McGary, R. S., & Elsenbeck, J. (2014). Electrical structure of the central Cascadia subduction zone: The EMSLAB Lincoln Line revisited. *Earth and Planetary Science Letters*, *402*, 265–274. https://doi.org/10.1016/j.epsl.2013.04.021

Fulton, P. M., Brodsky, E. E., Kano, Y., Mori, J., Chester, F., Ishikawa, T., & Toczko, S. (2013). Low coseismic friction on the Tohoku-Oki fault determined from temperature measurements. *Science*, *342*(6163), 1214–1217. https://doi.org/10.1126/science.1243641

Goldfinger, C., Nelson, C. H., & Johnson, J. E. (2003). Holocene earthquake records from the Cascadia Subduction Zone and northern San Andreas Fault Based on precise dating of offshore turbidites. *Annual Review of Earth and Planetary Sciences*, *31*(1), 555–577. https://doi.org/10.1146/annurev.earth.31.100901.141246

Gulick, S. P. S., Meltzer, A. M., & Clarke, S. H., Jr (1998). Seismic structure of the southern Cascadia subduction zone and accretionary prism north of the Mendocino triple junction. *Journal of Geophysical Research*, *103*(B11), 27207–27222. https://doi.org/10.1029/98JB02526

Guo, H., McGuire, J. J., & Zhang, H. (2018). Imaging the subducted Gorda plate: Implications for the stress state and brittle-ductile transition of the Cascadia subduction zone. AGU Fall Meeting Abstracts (Vol. 2018, T13H-0334).

Han, S., Bangs, N. L., Carbotte, S. M., Saffer, D. M., & Gibson, J. C. (2017). Links between sediment consolidation and Cascadia megathrust slip behavior. *Nature Geoscience*, *10*(12), 954–959. https://doi.org/10.1038/s41561-017-0007-2

Hayes, G. P., Moore, G. L., Portner, D. E., Hearne, M., Flamme, H., Furtney, M., & Smoczyk, G. M. (2018). Slab2, a comprehensive subduction zone geometry model. *Science*, *362*(6410), 58–61. https://doi.org/10.1126/science.aat4723

Horleston, A., & Helffrich, G. (2012). Constraining sediment subduction: A converted phase study of the Aleutians and Marianas. *Earth and Planetary Science Letters*, *359–360*, 141–151. https://doi.org/10.1016/j.epsl.2012.10.019

Hyndman, R. D. (2013). Downdip landward limit of Cascadia great earthquake rupture. *Journal of Geophysical Research: Solid Earth*, *118*, 5530–5549. https://doi.org/10.1002/jgrb.50390

Hyndman, R. D., & Wang, K. (1995). The rupture zone of Cascadia great earthquakes from current deformation and the thermal regime. *Journal of Geophysical Research*, *100*(B11), 22133–22154. https://doi.org/10.1029/95JB01970

Janiszewski, H. A., & Abers, G. A. (2015). Imaging the plate interface in the Cascadia seismogenic zone: New constraints from offshore receiver functions. *Seismological Research Letters*, *86*(5), 1261–1269. https://doi.org/10.1785/0220150104

Lay, T., Kanamori, H., Ammon, C. J., Koper, K. D., Hutko, A. R., Ye, L., & Rushing, T. M. (2012). Depth-varying rupture properties of subduction zone megathrust faults. *Journal of Geophysical Research*, *117*, B04311. https://doi.org/10.1029/2011JB009133

Li, D., McGuire, J. J., Liu, Y., & Hardebeck, J. L. (2018). Stress rotation across the Cascadia megathrust requires a weak subduction plate boundary at seismogenic depths. *Earth and Planetary Science Letters*, *485*, 55–64. https://doi.org/10.1016/j.epsl.2018.01.002

Liu, Y. (2013). Numerical simulations on megathrust rupture stabilized under strong dilatancy strengthening in slow slip region. *Geophysical Research Letters*, *40*, 1311–1316. https://doi.org/10.1002/grl.50298

Liu, Y., & Rice, J. R. (2005). Aseismic slip transients emerge spontaneously in three-dimensional rate and state modeling of subduction earthquake sequences. *Journal of Geophysical Research*, *110*, B08307. https://doi.org/10.1029/2004JB003424

Liu, Y., & Rice, J. R. (2007). Spontaneous and triggered aseismic deformation transients in a subduction fault model. *Journal of Geophysical Research*, *112*, B09404. https://doi.org/10.1029/2007JB004930

Lomnitz, C. (1982). Direct evidence of a subducted plate under southern Mexico. *Nature*, *296*(5854), 235–238. https://doi.org/10.1038/296235a0

Matsuzawa, T., Kono, T., Hasegawa, A., & Takagi, A. (1990). Subducting plate boundary beneath the northeastern Japan arc estimated from SP converted waves. *Tectonophysics*, *181*(1–4), 123–133. https://doi.org/10.1016/0040-1951(90)90012-W

Matsuzawa, T., Umino, N., Hasegawa, A., & Takagi, A. (1986, 09). Upper mantle velocity structure estimated from PS-converted wave beneath the north-eastern Japan Arc. *Geophysical Journal International*, *86*(3), 767–787. https://doi.org/10.1111/j.1365-246X.1986.tb00659.x

McCaffrey, R., King, R. W., Payne, S. J., & Lancaster, M. (2013). Active tectonics of northwestern U.S. inferred from GPS-derived surface velocities. *Journal of Geophysical Research: Solid Earth*, *118*, 709–723. https://doi.org/10.1029/2012JB009473

McCrory, P. A., Blair, J. L., Waldhauser, F., & Oppenheimer, D. H. (2012). Juan de Fuca slab geometry and its relation to Wadati-Benioff zone seismicity. *Journal of Geophysical Research*, *117*, B09306. https://doi.org/10.1029/2012JB009407

McGary, R. S., Evans, R. L., Wannamaker, P. E., Elsenbeck, J., & Rondenay, S. (2014). Pathway from subducting slab to surface for melt and fluids beneath Mount Rainier. *Nature*, *511*, 338. https://doi.org/10.1038/nature13493

Merrill, R., & Bostock, M. (2019, 08). An earthquake nest in Cascadia. *Bulletin of the Seismological Society of America*, *109*(5), 2021–2035. https://doi.org/10.1785/0120190055

Murray, M. H., Marshall, G. A., Lisowski, M., & Stein, R. S. (1996). The 1992 M 7 Cape Mendocino, California, earthquake: Coseismic deformation at the south end of the Cascadia megathrust. *Journal of Geophysical Research*, *101*(B8), 17707–17725. https://doi.org/10.1029/95JB02623

Nakamura, M., Ando, M., & Ohkura, T. (1998). Fine structure of deep Wadati Benioff zone in the Izu Bonin region estimated from S to P converted phase. *Physics of the Earth and Planetary Interiors*, *106*(1), 63–74. https://doi.org/10.1016/S0031-9201(97)00109-X

Nakata, N., & Shelly, D. R. (2018). Imaging a crustal low-velocity layer using reflected seismic waves from the 2014 earthquake swarm at Long Valley caldera, California: The magmatic system roof? *Geophysical Research Letters*, *45*, 3481–3488. https://doi.org/10.1029/2018GL077260

Nedimović, M. R., Hyndman, R. D., Ramachandran, K., & Spence, G. D. (2003, Jul 01). Reflection signature of seismic and aseismic slip on the northern Cascadia subduction interface. *Nature*, *424*(6947), 416–420. https://doi.org/10.1038/nature01840

Nowack, R. L., & Bostock, M. G. (2013). Scattered waves from low-frequency earthquakes and plate boundary structure in northern Cascadia. *Geophysical Research Letters*, *40*, 4238–4243. https://doi.org/10.1002/grl.50826

Obara, K., & Sato, H. (1988). Existence of an S wave reflector near the upper plane of the double seismic zone beneath the Southern Kanto District, Japan. *Journal of Geophysical Research*, *93*(B12), 15037–15045. https://doi.org/10.1029/JB093iB12p15037

Ohmi, S., & Hori, S. (2000). Seismic wave conversion near the upper boundary of the Pacific plate beneath the Kanto district, Japan. *Geophysical Journal International*, *141*(1), 136–148. https://doi.org/10.1046/j.1365-246X.2000.00086.x

Peacock, S. M., Christensen, N. I., Bostock, M. G., & Audet, P. (2011). High pore pressures and porosity at 35 km depth in the Cascadia subduction zone. *Geology*, *39*(5), 471–474. https://doi.org/10.1130/G31649.1

Petersen, M. D., Moschetti, M. P., Powers, P. M., Mueller, C. S., Haller, K. M., Frankel, A. D., & Olsen, A. H. (2014). *2014 update of the U.S. national seismic hazard maps*. Reston, VA: USGS National Seismic Hazard Mapping Project. Retrieved from http://pubs.er.usgs.gov/publication/70096755

Peterson, D. E., & Keranen, K. M. (2019). A high wave speed basal sedimentary layer identified from seismic imaging of the plate boundary in central Cascadia. *Journal of Geophysical Research: Solid Earth*, *124*, 6832–6847. https://doi.org/10.1029/2018JB017227

Pimienta, L., Schubnel, A., Violay, M., Fortin, J., Guéguen, Y., & Lyon-Caen, H. (2018). Anomalous Vp/Vs ratios at seismic frequencies might evidence highly damaged rocks in subduction zones. *Geophysical Research Letters*, *45*, 12210–12217. https://doi.org/10.1029/2018GL080132

Pollitz, F., & Evans, E. (2017, 01). Implications of the earthquake cycle for inferring fault locking on the Cascadia megathrust. *Geophysical Journal International*, *209*(1), 167–185. https://doi.org/10.1093/gji/ggx009

Ramos, M. D., & Huang, Y. (2019). How the transition region along the Cascadia megathrust influences coseismic behavior: Insights from 2-D dynamic rupture simulations. *Geophysical Research Letters*, *46*, 1973–1983. https://doi.org/10.1029/2018GL080812

Reading, A. M., Gubbins, D., & Mao, W. (2001, 09). A multiphase seismic investigation of the shallow subduction zone, southern North Island, New Zealand. *Geophysical Journal International*, *147*(1), 215–226. https://doi.org/10.1046/j.1365-246X.2001.00500.x

Rogers, G., & Dragert, H. (2003). Episodic tremor and slip on the Cascadia subduction zone: The chatter of silent slip. *Science*, *300*(5627), 1942–1943. https://doi.org/10.1126/science.1084783

Rubinstein, J. L., Vidale, J. E., Gomberg, J., Bodin, P., Creager, K. C., & Malone, S. D. (2007). Non-volcanic tremor driven by large transient shear stresses. *Nature*, *448*(7153), 579–582. https://doi.org/10.1038/nature06017

Saffer, D. M., & Tobin, H. J. (2011). Hydrogeology and mechanics of subduction zone forearcs: Fluid flow and pore pressure. *Annual Review of Earth and Planetary Sciences*, *39*(1), 157–186. https://doi.org/10.1146/annurev-earth-040610-133408

Savard, G., Bostock, M. G., & Christensen, N. I. (2018). Seismicity, metamorphism, and fluid evolution across the northern Cascadia fore arc. *Geochemistry, Geophysics, Geosystems*, *19*, 1881–1897. https://doi.org/10.1029/2017GC007417

Schmalzle, G. M., McCaffrey, R., & Creager, K. C. (2014). Central Cascadia subduction zone creep. *Geochemistry, Geophysics, Geosystems*, *15*, 1515–1532. https://doi.org/10.1002/2013GC005172

Segall, P., & Bradley, A. M. (2012). Slow-slip evolves into megathrust earthquakes in 2d numerical simulations. *Geophysical Research Letters*, *39*, L18308. https://doi.org/10.1029/2012GL052811

Song, T.-R. A., Helmberger, D. V., Brudzinski, M. R., Clayton, R. W., Davis, P., Pérez-Campos, X., & Singh, S. K. (2009). Subducting slab ultra-slow velocity layer coincident with silent earthquakes in southern Mexico. *Science*, *324*(5926), 502–506. https://doi.org/10.1126/science.1167595

Song, T.-R. A., & Kim, Y. (2011). Anisotropic uppermost mantle in young subducted slab underplating Central Mexico. *Nature Geoscience*, *5*, 55–59. https://doi.org/10.1038/ngeo1342

Spudich, P., & Bostwick, T. (1987). Studies of the seismic coda using an earthquake cluster as a deeply buried seismograph array. *Journal of Geophysical Research*, *92*(B10), 10526–10546. https://doi.org/10.1029/JB092iB10p10526

Stephenson, W. J., Reitman, N. G., & Angster, S. J. (2017). *P- and S-wave velocity models incorporating the Cascadia subduction zone for 3D earthquake ground motion simulations, version 1.6—Update for Open-File Report 2007-1348 (ver. 1.1, Sept. 10, 2019)*. U.S. Geological Survey Open-File Report 2017-1152, 17 p., https://doi.org/10.3133/ofr20171152

Stephens, C. D., Page, R. A., & Lahr, J. C. (1990). Reflected and mode-converted seismic waves within the shallow Aleutian Subduction Zone, Southern Kenai Peninsula, Alaska. *Journal of Geophysical Research*, *95*(B5), 6883–6897. https://doi.org/10.1029/JB095iB05p06883

Tauzin, B., Reynard, B., Perrillat, J.-P., Debayle, E., & Bodin, T. (2017). Deep crustal fracture zones control fluid escape and the seismic cycle in the Cascadia subduction zone. *Earth and Planetary Science Letters*, *460*, 1–11. https://doi.org/10.1016/j.epsl.2016.12.007

Thorwart, M. (2006). *Wavefield methods to analyze passive ocean bottom seismic data—Application to the Tyrrhenian Sea. PhD thesis*. University of Hamburg. Retrieved from https://webdoc.sub.gwdg.de/ebook/dissts/Hamburg/Thorwart2006.pdf

Toomey, D. R., Allen, R. M., Barclay, A. H., Bell, S. W., Bromirski, P. D., Carlson, R. I., & Wilcock, W. S. (2014). The Cascadia Initiative: A sea change in seismological studies of subduction zones. *Oceanography*, *27*(2), 138–150.

Tréhu, A. M., & Group, M. W. (1995). Pulling the rug out from under California: Seismic images of the Mendocino Triple Junction Region. *Eos, Transactions American Geophysical Union*, *76*(38), 369–381. https://doi.org/10.1029/95EO00229

Tromp, J., Komatitsch, D., & Liu, Q. (2008). Spectral-element and adjoint methods in seismology. *Communications in Computational Physics*, *3*(1), 1–32.

Um, J., & Thurber, C. (1987). A fast algorithm for two-point seismic ray tracing. *Bulletin of the Seismological Society of America*, *77*(3), 972–986.

Wang, K., & Tréhu, A. M. (2016). Invited review paper: Some outstanding issues in the study of great megathrust earthquakes? The Cascadia example. *Journal of Geodynamics*, *98*, 1–18. https://doi.org/10.1016/j.jog.2016.03.010

Wannamaker, P. E., Evans, R. L., Bedrosian, P. A., Unsworth, M. J., Maris, V., & McGary, R. S. (2014). Segmentation of plate coupling, fate of subduction fluids, and modes of arc magmatism in Cascadia, inferred from magnetotelluric resistivity. *Geochemistry, Geophysics, Geosystems*, *15*, 4230–4253. https://doi.org/10.1002/2014GC005509

Wech, A. G., & Creager, K. C. (2011, Aug 07). A continuum of stress, strength and slip in the Cascadia subduction zone. *Nature Geoscience*, *4*, 624. https://doi.org/10.1038/ngeo1215

Wirth, E. A., Frankel, A. D., Marafi, N., Vidale, J. E., & Stephenson, W. J. (2018, 08). Broadband synthetic seismograms for magnitude 9 earthquakes on the Cascadia megathrust based on 3D simulations and stochastic synthetics, Part 2: Rupture parameters and variability. *Bulletin of the Seismological Society of America*, *108*(5A), 2370–2388. https://doi.org/10.1785/0120180029

Zhang, H., & Thurber, C. H. (2003). Double-Difference tomography: The method and its application to the Hayward fault, California. *Bulletin of the Seismological Society of America*, *93*(5), 1875–1889. https://doi.org/10.1785/012000270

Zhu, L., & Rivera, L. A. (2002, 03). A note on the dynamic and static displacements from a point source in multilayered media. *Geophysical Journal International*, *148*(3), 619–627. https://doi.org/10.1046/j.1365-246X.2002.01610.x